

NASA  
Technical Memorandum 106069

Army Research Laboratory  
Memorandum Report ARL-MR-69

# Spray Combustion Experiments and Numerical Predictions

1N-34  
157727  
p 23

Edward J. Mularz  
*Vehicle Propulsion Directorate*  
*U.S. Army Research Laboratory*  
*Lewis Research Center*  
*Cleveland, Ohio*

Daniel L. Bulzan  
*Lewis Research Center*  
*Cleveland, Ohio*

and

Kuo-Huey Chen  
*University of Toledo*  
*Toledo, Ohio*

(NASA-TM-106069) SPRAY COMBUSTION  
EXPERIMENTS AND NUMERICAL  
PREDICTIONS (NASA) 23 p

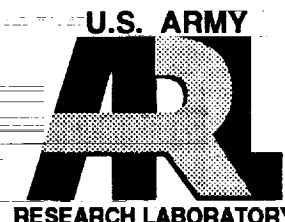
N93-23744

Unclass

G3/34 0157727

Prepared for the  
AGARD Symposium on Fuels and Combustion Technology  
for Advanced Gas Turbine Engines  
sponsored by the Advisory Group for Aerospace Research and Development  
Colleferro, Nr. Rome, Italy, Spring 1993

**NASA**





## SPRAY COMBUSTION EXPERIMENTS AND NUMERICAL PREDICTIONS

Dr. Edward J. Mularz  
Vehicle Propulsion Directorate  
U.S. Army Research Laboratory  
Lewis Research Center  
Cleveland, Ohio 44135

Dr. Daniel L. Bulzan  
National Aeronautics and Space Administration  
Lewis Research Center  
Cleveland, Ohio 44135

and

Dr. Kuo-Huey Chen  
University of Toledo  
Toledo, Ohio 43606

### SUMMARY

The next generation of commercial aircraft will include turbofan engines with performance levels significantly better than those in the current fleet. Control of particulate and gaseous emissions will also be an integral part of the engine design criteria. These performance and emission requirements present a technical challenge for the combustor: control of the fuel and air mixing and control of the local stoichiometry will have to be maintained much more rigorously than with combustors in current production. A better understanding of the flow physics of liquid fuel spray combustion is necessary. This paper describes recent experiments on spray combustion where detailed measurements of the spray characteristics were made, including local drop-size distributions and velocities. Also, an advanced combustor CFD code has been under development and predictions from this code are compared with experimental results. Studies such as these will provide information to the advanced combustor designer on fuel spray quality and mixing effectiveness. Validation of new fast, robust, and efficient CFD codes will also enable the combustor designer to use them as valuable additional design tools for optimization of combustor concepts for the next generation of aircraft engines.

### A. INTRODUCTION

Aircraft engines being envisioned now for the next-century aircraft will have requirements that present formidable technical challenges to the combustor designer. In the subsonic commercial transport arena, demand for low operating cost translates into reduced fuel consumption and improved durability and reliability. Higher operating pressures of the combustor are forecast, with higher resulting fuel system turn-down ratios. Coupled with these performance requirements is the demand world wide for control of pollutant emissions from aircraft engines, especially oxides of nitrogen. In the arena of supersonic commercial transports, forecasts are

predicting fleets of hundreds of transports operating at Mach 2.0 to 2.5, with airfares only slightly higher than today's long-range subsonic fares. Economical fuel consumption is a requirement. But the largest technical challenge here is low levels of oxides of nitrogen emissions during engine cruise such that there would be no adverse impact to the earth's environment, specifically the atmosphere's ozone layer.

These technical and environmental challenges represent design requirements for the combustor that are outside of engine companies' experience. Empirically based design methods are insufficient by themselves. To augment this design system, the companies are increasingly turning to computational fluid dynamics (CFD) computer codes. Severe limitations with currently available codes are excessive time requirements to run a CFD code to analyze a complex combustor design: a penalty both in turn-around time for design answers as well as cost for the calculations. We at NASA are attempting to improve this current situation in the industry by developing a fast, robust, efficient computer code for internal chemical reacting flows. The objective is to produce a CFD code that can be used as a more powerful design tool in the industry to analyze complex combustor designs in significantly shorter turn-around time than current computer codes can achieve.

An integral part of the development of a new CFD code is the validation of this code with experiments that represent the complex features of the flows which need to be analyzed. Therefore, at NASA we are also conducting experiments on liquid fuel spray combustor flows with increasingly complex features. This will provide some of the required data for validation of our CFD code and other's codes. Detailed measurements of both liquid sprays and gas characteristics are being obtained under both nonburning and burning conditions.

This paper will highlight recent results that NASA has obtained with its spray combustion experiment and describe

the formulation and physical modeling of its new spray combustion CFD code (ALLSPD). The application of this code to combustion problems will be illustrated by several examples.

## B. SPRAY COMBUSTION EXPERIMENTS

Combusting sprays are very important for gas turbine engine applications. The investigation of combusting sprays should lead to a better understanding of the physics involved in this complicated process. Important processes involved in combusting sprays are the interactions between the droplets and the gas phase, the vaporization of the droplets, and chemical reactions with heat release. These physical processes are coupled and can only be completely described using numerical modeling. As part of an effort to improve the numerical modeling of gas turbine combustors, an experimental study has been undertaken to obtain a data set for a relatively simple liquid-fueled combustor that can be used for comparison with numerical models (Ref. 1).

Because of their practical applications, swirling flows with combustion have been studied by a large number of investigators. Earlier reviews of swirling flows both with and without combustion present some general trends (Refs. 2 to 4). These papers predate the development of nonintrusive, laser-based diagnostics; consequently all of the results described were obtained using intrusive instrumentation and detailed structure measurements for these types of flows were not possible. With the advent of newer instrumentation techniques, namely laser Doppler anemometry, additional details of the structure of these types of flows began to emerge. Laser Doppler anemometry velocity measurements in spray flames (Refs. 5 and 6) reveal some of the flowfield structure of swirling flames. The development of the phase/Doppler particle analyzer (Ref. 7), enabled the simultaneous measurement of droplet size and velocity. This instrument has been used by a number of investigators for measurements in spray flames in a variety of configurations (Refs. 8 to 12). This instrument has the capability to measure velocities of both the gas and droplet phases in a combusting spray.

### B.1 EXPERIMENT

The combustor utilized in the present experiment is illustrated in Fig. 1. It consists of a center mounted air-assist fuel nozzle, Parker Hannifin research simplex air-assist atomizer, surrounded by a coflowing air stream. The nozzle orifice diameter was 4.8 mm. Both the air assist and the coflow air streams had swirl imparted to them using 45 degree swirlers. The swirlers were constructed by machining 45 degree slots into rings. Both streams were swirled in the same direction for the present study. The combustion air was not preheated and entered the combustor at 297 K. The top of the air-assist nozzle was water cooled to prevent overheating of an O-ring in the nozzle assembly. The temperatures of the fuel, atomizing air and coflow air streams were measured using Chromal Alumel thermocouples. Flow rates of the air streams were measured using calibrated orifices and the fuel flow rate was measured using a mass flowmeter. All results reported in the present study are reported for a coflow air flow rate of 13.88 g/s, an air-assist flow rate of 0.96 g/s, and a fuel flow rate of 0.38 g/s. The fuel used was heptane. The coflow

stream entered the combustor in three radial locations, passed through a honeycomb flow straightener, and the swirlers before exiting the combustor. The swirler was located 140 mm upstream of the combustor exit. The flow from the combustor discharged into ambient, stagnant surroundings.

The combustor was mounted vertically within a large (1.8 m sq by 2.4 m high) enclosure. The entire enclosure was mounted on two sets of linear bearings and was traversed using stepper motors to provide motion in two directions. The combustor assembly itself could be traversed in the vertical direction using a third stepper motor to allow measurements at all locations in the flowfield. This arrangement allowed rigid mounting of all optical components.

The phase/Doppler particle analyzer was used for all measurements reported in this study. A schematic of the two-component instrument is shown in Fig. 2. The beam from a 6 W Argon-ion laser is split into 488.0 and 514.5 nm wavelengths using a dichroic mirror. Each beam is then focused onto a rotating diffraction grating which splits each beam into several pairs. The two first-order beams for each wavelength are then recombined onto the optical axis using a dichroic mirror, collimated and focused at a point to form the two-component probe volume. In the present study, the transmitting optics utilized a 500 mm focal length lens. The receiving optics were located 30 degrees off axis in the forward-scatter direction. Light was collected using a 500 mm focal-length lens and then focused onto a 100  $\mu$ m by 1 mm long slit. The collected light is then split and picked up by four photodetectors. Three are arranged to look at the signals from the 514.5 beams and one receives light from the 488 nm beams. Each of the three photodetectors for the green beams are imaged at a different area of the collection lens and the phase difference between the signals is used for the size determination. Details of the instrument can be found in Ref. 7.

In the present study, velocities of both the liquid and gaseous phases were measured. This was accomplished by seeding the gas phase with nominal 1  $\mu$ m size aluminum-oxide particles. The coflow, air-assist flow, and the ambient surroundings were all seeded to minimize biasing. Phase discrimination is inherent in the instrumentation with the ability to size each measured particle. At each spatial location, two measurements were taken in order to accurately measure the velocity of each phase. A threshold voltage for the photodetectors at the specified laser power was determined experimentally, below which signals from the aluminum-oxide particles were not detected. For the droplet measurements, the photodetector voltage was kept below this threshold value in order to eliminate interference from the aluminum-oxide particles. Total laser power for all wavelengths was fixed at 1.5 W for all the measurements. Particles with diameters less than 2.4  $\mu$ m were used to represent the gas phase velocity. Two complete traverses were taken in order to measure all three components of velocity and provide a check on flow symmetry. Each traverse measured axial velocity and either radial or angular velocity. Generally, 64 000 measurement attempts were made at each measurement location. The percentage of measurements actually validated depended on the number density and velocities of drops at each location and ranged from about 65 to 90 percent.

## B.2 RESULTS AND DISCUSSION

In the present study, results are presented for a single axial location at 5 mm downstream of the nozzle. Gas phase results for mean velocities are presented in Figs. 3(a) to (c) for isothermal, single-phase flow without droplets and two-phase flow with combustion. Mean gas phase axial velocity, presented in Fig. 3(a), presents results from a complete traverse across the combustor and illustrates the symmetry of the flowfield. The combustor exit dimensions are illustrated on the x-axis of the figure for reference. A small recirculation zone is evident near the center of the nozzle. At this axial location relatively close to the nozzle, velocity gradients are extremely large in the flow from the air-assist stream containing the droplets. Effects of combustion on the flowfield are significant. Both the maximum and minimum mean axial velocities are increased for the combustor case compared to the isothermal case due to the gas expansion associated with the heat release. For the case with combustion, velocities increase from nearly 0 to 35 m/s and then decrease to -30 m/s within a radius of about 12 mm. Mean axial velocities in the coflow stream are not affected by the combustion at this axial location.

Figure 3(b) presents mean radial velocity for the gas phase. As shown in Fig. 3(b), effects of combustion are very dramatic for radial velocity. Maximum radial velocities increased from about 10 m/s for the isothermal case to about 40 m/s for the case with combustion due to the radial expansion of the gas. Again, the gas from the coflow stream is not affected by the combustion at this axial location.

Mean gas phase angular velocities are presented in Fig. 3(c). For this case, reaction and the presence of droplets decreases the maximum angular velocities in the flowfield. Some of the decrease in angular velocity for the gas phase can be attributed to the momentum transferred to the droplets since they do not initially have a swirl component.

Fluctuating gas phase velocities are presented in Figs. 4(a) to (c) for both the single-phase, isothermal and the two-phase, combustor cases. All fluctuating velocities presented are root-mean-squared (rms) values. Figure 4(a) presents radial profiles of gas phase fluctuating axial velocity. Maximum values of fluctuating axial velocity are similar for both the combustor and isothermal cases. The case with combustion does show larger values of axial rms velocity at radial locations between approximately 5 and 15 mm from the center of the nozzle. Axial velocities are also higher at these locations for the combustor case, see Fig. 3(a). Fluctuating radial velocities, illustrated in Fig. 4(b), show dramatic differences between the isothermal and combustor cases. The maximum velocity locations have shifted radially outward corresponding to the shift in mean radial velocity, see Fig. 3(b). The maximum fluctuating radial velocity has also increased from about 10 m/s to 15 m/s.

Fluctuating angular gas phase velocities are presented in Fig. 4(c). Similar to the results shown for mean angular gas phase velocities, fluctuating angular velocities generally decreased with combustion and the presence of the liquid phase compared to the single-phase, isothermal case. A small region from a radius of about 7 to 15 mm shows increased values of fluctuating angular velocity for the case with combustion.

Mean velocities for the drops are presented in Figs. 5(a) to (c) for the case with combustion. In the experimental study, velocities were measured for drop sizes ranging from 4 to 142  $\mu\text{m}$ . Results are presented for drop sizes of 15, 32 and 52  $\mu\text{m}$ . Measured gas phase velocities are also presented in the figure. Note that results are only illustrated from -15 to +15 mm for the radial direction because no drops were present at larger radial locations. Figure 5(a) presents mean drop axial velocity at 5 mm downstream. Similar to the results previously shown for the gas phase, the flowfield is very symmetric. Axial velocity is correlated with drop size in all regions. In the main region of the spray, at a radius of about 7 mm, the maximum velocity of the gas phase was about 38 m/s, and about 28 m/s for the 32  $\mu\text{m}$  drops. Even the maximum velocity of the 15  $\mu\text{m}$  drops lagged the gas phase by about 5 m/s. In the center of the flowfield is a small recirculation zone, see Fig. 3(a). There, only the 15  $\mu\text{m}$  drops showed negative axial velocities while larger drops had positive velocities.

Mean drop radial velocities are presented in Fig. 5(b). Again, there is a correlation between drop size and velocity in the flowfield. Maximum mean radial velocities are slightly higher than maximum axial velocities for the drops due to the heat release and radial expansion of the gas. Mean angular velocities of the drops are presented in Fig. 5(c). Angular velocity is not as symmetric and is also much smaller than the other two components of velocity. The mean drop angular velocity is a strong function of the drop size with the smaller drops showing the least velocity difference with the gas phase.

Fluctuating droplet axial, radial, and angular velocity components for the three drop sizes and gas phase are presented in Figs. 6(a) to (c), respectively. The fluctuating drop velocities presented are root-mean-squared (rms) values. Generally, the smaller drops are affected more by the gas phase turbulence and have larger fluctuating velocities than the larger drops. Velocity fluctuations are clearly not isotropic since fluctuating axial and radial velocities are considerably larger than fluctuating angular velocities.

In addition to drop mean and fluctuating velocities, the liquid volume flux is important in two-phase flows. Drop number-flux measurements are presented in Fig. 7, where results are illustrated for four drop size groups. As shown in Fig. 7, number flux is nearly symmetric. The results show that smaller droplets have much larger number fluxes. The distribution of the larger droplets is still very important since much of the liquid mass is contained in the larger droplets. Relatively few drops are found in the center region of the flowfield due to the 45 degree swirler that is used in the air-assist stream.

## C. COMBUSTION CFD CODE

The objective of the present work is to develop a numerical solution procedure which can efficiently handle the coupling between a spray model and a well-developed strongly implicit flow solution algorithm (Refs. 13 and 14). In the past, spray models have been coupled with different flow algorithms and shown some promising results (Refs. 15 to 17). However, most of the spray models were coupled with a flow solver employing a segregated approach, such as a TEACH-type code (Refs. 15 and 16), which has been used very extensively in the industries for the past two decades. Although simple

and easy to implement, the TEACH-type code usually suffers poor convergence due to the explicit (or semi-implicit) treatments of the chemical source terms and the sequential solution approach. Recent development of CFD techniques and the advent of computer technology have allowed us to explore more ambitious schemes to solve reacting flow problems. Strongly coupled and implicit numerical schemes, although requiring much more computer storage and complexity of the algorithm, have been very popular for nonreacting compressible (Refs. 18 and 19) and incompressible (Refs. 20 and 21) flow computations.

Shuen and Yoon (Ref. 22) developed a coupled scheme for high speed reacting flows, RPLUS, which has been used and studied quite extensively in recent years. However, like other compressible flow solution algorithms, RPLUS may not be suitable for low speed flow computations. There are two well-recognized reasons (Refs. 23 to 25) for the convergence difficulties related to compressible flow codes. First, the system's eigenvalues become stiff at low flow velocities. Second, the pressure term in the momentum equation becomes singular as the Mach number approaches zero, which yields a large roundoff error and smears the pressure variation field. This will not only result in slow convergence but often will produce inaccurate solutions. To circumvent the above difficulties, Shuen et al. (Ref. 13) developed a coupled numerical algorithm for chemical nonequilibrium viscous flows, ALLSPD, which utilizes the decomposition of the pressure variable into a constant reference pressure and a gauge pressure to reduce the roundoff errors and adds a preconditioning time derivative term to rescale the system eigenvalues. The results of these treatments show that the convergence properties are almost independent of the flow Mach number.

Numerous spray models have been proposed and investigated for different spray combustion problems (Refs. 26 and 27) in the past decade. Recent spray models differ in specific details, but generally may be divided into two categories: locally homogeneous flow (LHF) models and separated flow (SF) models. LHF models represent the simplest treatment of a multiphase flow and have been widely used to analyze sprays (Ref. 28). The key assumption of the LHF model is that interphase transport rates are fast in comparison to the rate of development of the flow. This implies that all phases have identical properties at each point in the flow. Clearly, LHF models are only formally correct for flows containing infinitely small droplets.

Numerous SF models have been proposed to consider interphase transport phenomena (Ref. 29). Among them, the discrete droplet approach (Refs. 26 and 30) has been adopted, since it reduces numerical diffusion while providing a convenient framework for dealing with multiple droplet size and complex interphase transport phenomena. Many discrete droplet models neglect the effects of turbulence on interphase transport (Refs. 26 and 30). This implies that droplets follow deterministic trajectories, yielding the deterministic separated flow (DSF) model. Neglecting the effects of turbulence on droplet transport is appropriate when characteristic droplet relaxation times are large in comparison to characteristic times of turbulent fluctuations. Few practical sprays, however, satisfy this condition. Dukowicz (Ref. 31) and Gosman and Ioannides (Ref. 32) have adopted stochastic methods to study droplet dispersion by turbulence. Faeth and coworkers

(Ref. 33) extended the analysis of Gosman et al. to include the effects of turbulence on interphase heat and mass transport. Their stochastic separated flow (SSF) model (Ref. 33) has been evaluated in a wide variety of parabolic flows with very encouraging results.

In a recent paper (Ref. 34), the ALLSPD algorithm was extended to include a SSF spray model (Ref. 33), a recently developed low Reynolds number  $\kappa$ - $\epsilon$  turbulence model (Ref. 35) and a multiblock treatment to calculate the gas turbine combustion flows, where the liquid spray is an important ingredient of combustion. Although the turbulence model has been included in this study for turbulent combustion flow calculations, the mean flow quantities are still used in the chemistry calculations. The turbulence closure problem for chemistry is more complicated and computationally intensive. The consideration of a suitable turbulent combustion closure model is left for our next-phase study in the near future.

In this paper, in addition to the gas turbine spray combustion flow, a single-phase premixed turbulent combustion flow and a nonreacting turbulent flow are also included to demonstrate the current status of this research. In the following sections, a brief mathematical formulation of the governing equations for both gas and liquid-phases is described. The numerical method and discretization procedure are given next and finally some sample numerical results are presented.

## C.1 GOVERNING EQUATIONS

### C.1a Gas-Phase Equations

#### C.1a(i) Navier-Stokes Formulation

The two-dimensional, unsteady, compressible, density-weighted time-averaged Navier-Stokes equations and species transport equations for a chemically reacting gas of  $N$  species written in generalized nonorthogonal coordinates can be expressed as

$$\frac{\partial \bar{Q}}{\partial \tau} + \frac{\partial (\bar{E} - \bar{E}_v)}{\partial \xi} + \frac{\partial (\bar{F} - \bar{F}_v)}{\partial \eta} = \bar{H}_c + \bar{H}_l \quad (1)$$

where the vectors  $\bar{Q}$ ,  $\bar{E}$ ,  $\bar{F}$ ,  $\bar{E}_v$ ,  $\bar{F}_v$ ,  $\bar{H}_c$ , and  $\bar{H}_l$  are defined as

$$\begin{aligned} \bar{Q} &= \frac{1}{J} Q, \\ \bar{E} &= \frac{1}{J} (\xi_x Q + \xi_x E + \xi_y F), \\ \bar{F} &= \frac{1}{J} (\eta_x Q + \eta_x E + \eta_y F), \\ \bar{E}_v &= \frac{1}{J} (\xi_x E_v + \xi_y F_v), \\ \bar{F}_v &= \frac{1}{J} (\eta_x E_v + \eta_y F_v), \\ \bar{H}_c &= \frac{1}{J} H_c, \\ \bar{H}_l &= \frac{1}{J} H_l. \end{aligned}$$

In the above expressions,  $\tau$ ,  $\xi$ , and  $\eta$  are the time and spatial coordinates in the generalized coordinates and  $\xi_x$  and  $\eta_x$  are the grid speed terms. The  $\xi_x$ ,  $\xi_y$ ,  $\eta_x$ , and  $\eta_y$  are the metric terms and the  $J$  is the transformation Jacobian. The power,  $\delta$ ,

is an index for two types of governing equations with  $\delta = 0$  for two-dimensional and  $\delta = 1$  for axisymmetric cases (with  $x$  being the axial and  $y$  the radial coordinates, respectively). The vectors  $Q$ ,  $E$ ,  $F$ ,  $E_v$ ,  $F_v$ ,  $H_e$  and  $H_l$  in the above definitions are

$$Q = (\rho, \rho u, \rho v, \rho E, \rho \kappa, \rho \epsilon, \rho Y_1, \dots, \rho Y_{N-1})^T,$$

$$E = (\rho u, \rho u^2 + p, \rho uv, (\rho E + p)u, \rho u \kappa, \\ \times \rho u \epsilon, \rho u Y_1, \dots, \rho u Y_{N-1})^T,$$

$$F = (\rho v, \rho uv, \rho v^2 + p, (\rho E + p)v, \rho v \kappa, \\ \times \rho v \epsilon, \rho v Y_1, \dots, \rho v Y_{N-1})^T,$$

$$E_v = (0, \tau_{xx}, \tau_{xy}, u\tau_{xx} + v\tau_{xy} + q_{xe}, \tau_{x\kappa}, \\ \times \tau_{x\epsilon}, q_{x1}, \dots, q_{xN-1})^T,$$

$$F_v = (0, \tau_{yx}, \tau_{yy}, u\tau_{yx} + v\tau_{yy} + q_{ye}, \tau_{y\kappa}, \\ \times \tau_{y\epsilon}, q_{y1}, \dots, q_{yN-1})^T,$$

and the source term vectors  $H_e$  and  $H_l$  are

$$H_e = \begin{pmatrix} 0 \\ -\frac{2}{3} \delta \frac{\partial(\mu_e v)}{\partial x} \\ \delta \left[ p - \tau_{\theta\theta} - \frac{2}{3} \frac{\partial(\mu_e v)}{\partial y} \right] \\ -\frac{2}{3} \delta \left[ \frac{\partial(\mu_e uv)}{\partial x} + \frac{\partial(\mu_e v^2)}{\partial y} \right] \\ y^\delta (\Psi - \rho \epsilon) - \frac{2}{3} \delta \mu_e v \left( \frac{\partial u}{\partial x} + \frac{\partial v}{\partial y} \right) \\ y^\delta \left[ (c_1 f_1 \Psi - c_2 f_2 \rho \kappa) \frac{\epsilon}{\kappa} + \Lambda \right] - \frac{2}{3} \delta \mu_e v \\ \times \left( \frac{\partial u}{\partial x} + \frac{\partial v}{\partial y} \right) c_1 f_1 \frac{\epsilon}{\kappa} \\ y^\delta S_1 \\ \vdots \\ y^\delta S_{N-1} \end{pmatrix}.$$

and

$$H_l = \begin{pmatrix} \sum_p n_p \dot{m}_p \\ \sum_p n_p \dot{m}_p u_p - \frac{4\pi}{3} \rho_p r_p^3 n_p \frac{du_p}{dt} \\ \sum_p n_p \dot{m}_p v_p - \frac{4\pi}{3} \rho_p r_p^3 n_p \frac{dv_p}{dt} \\ \sum_p n_p \dot{m}_p h_{fs} - 4\pi r_p^2 n_p h \Delta T \\ 0 \\ 0 \\ \sum_p n_p \dot{m}_p \\ \vdots \\ 0 \end{pmatrix}.$$

where  $\rho$ ,  $p$ ,  $u$ ,  $v$ ,  $\kappa$ ,  $\epsilon$ , and  $Y_i$  represent the density, pressure, Cartesian velocity components, turbulent kinetic energy, dissipation rate of turbulent kinetic energy and species mass fraction, respectively;  $E = e + \frac{1}{2}(u^2 + v^2)$  is the total internal energy with  $e$  being the thermodynamic internal energy; and  $S_i$  is the rate of change of species  $i$  due to chemical reactions. The normal and shear stresses, energy, species, and turbulent diffusion fluxes are given by

$$\tau_{xx} = 2\mu_e \frac{\partial u}{\partial x} - \frac{2}{3} \mu_e \left( \frac{\partial u}{\partial x} + \frac{\partial v}{\partial y} \right),$$

$$\tau_{xy} = \mu_e \left( \frac{\partial u}{\partial y} + \frac{\partial v}{\partial x} \right),$$

$$\tau_{yy} = 2\mu_e \frac{\partial v}{\partial y} - \frac{2}{3} \mu_e \left( \frac{\partial u}{\partial x} + \frac{\partial v}{\partial y} \right),$$

$$\tau_{\theta\theta} = \frac{4}{3} \mu_e \frac{v}{y} - \frac{2}{3} \mu_e \left( \frac{\partial u}{\partial x} + \frac{\partial v}{\partial y} \right),$$

$$q_{xe} = k_e \frac{\partial T}{\partial x} + \rho \sum_{i=1}^N h_i D_{im} \frac{\partial Y_i}{\partial x},$$

$$q_{ye} = k_e \frac{\partial T}{\partial y} + \rho \sum_{i=1}^N h_i D_{im} \frac{\partial Y_i}{\partial y},$$

$$\tau_{x\kappa} = \left( \mu_l + \frac{\mu_r}{\sigma_\kappa} \right) \frac{\partial \kappa}{\partial x},$$

$$\tau_{y\kappa} = \left( \mu_l + \frac{\mu_r}{\sigma_\kappa} \right) \frac{\partial \kappa}{\partial y},$$

$$\tau_{x\epsilon} = \left( \mu_l + \frac{\mu_r}{\sigma_\epsilon} \right) \frac{\partial \epsilon}{\partial x}.$$

$$\tau_{ye} = \left( \mu_l + \frac{\mu_t}{\sigma_e} \right) \frac{\partial e}{\partial y},$$

$$q_{xl} = \rho D_{lm} \frac{\partial Y_l}{\partial x},$$

$$q_{yl} = \rho D_{lm} \frac{\partial Y_l}{\partial y},$$

where  $T$ ,  $\mu_e$ ,  $\mu_t$ ,  $\mu_l$  and  $k_e$  are the temperature, effective viscosity, turbulent viscosity, molecular viscosity and the effective thermal conductivity, respectively;

$$D_{lm} = (1 - X_l) \sum_{j=1}^N X_j D_{lj}$$

is the effective binary diffusivity of species  $i$  in the gas mixture,  $X_i$  the molar fraction of species  $i$ , and  $D_{ij}$  the binary mass diffusivity between species  $i$  and  $j$ . The quantities related to the source term in the turbulent equations are given as

$$\begin{aligned} \Psi = \mu_t & \left\{ \left[ 2 \frac{\partial u}{\partial x} - \frac{2}{3} \left( \frac{\partial u}{\partial x} + \frac{\partial v}{\partial y} \right) \right] \frac{\partial u}{\partial x} + \left[ 2 \frac{\partial v}{\partial y} - \frac{2}{3} \right. \right. \\ & \left. \left. \times \left( \frac{\partial u}{\partial x} + \frac{\partial v}{\partial y} \right) \right] \frac{\partial v}{\partial y} + \left( \frac{\partial u}{\partial x} + \frac{\partial v}{\partial y} \right)^2 \right\} \\ & - \frac{2}{3} \rho \kappa \left( \frac{\partial u}{\partial x} + \frac{\partial v}{\partial y} \right). \end{aligned}$$

$$\Lambda = \nu \mu_t \frac{\partial^2 u}{\partial y^2},$$

and

$$\begin{aligned} c_1 = 1.44, \quad c_2 = 1.92, \quad f_1 = 1.00, \\ \times f_2 = 1 - 0.22 \exp \left( -R_t^2/36 \right), \\ \times \sigma_k = 1, \end{aligned}$$

$$\begin{aligned} \sigma_e = 1.3, \quad R_t = \frac{\kappa^2}{\nu e}, \quad \mu_e = \mu_l + \mu_t, \\ \times k_e = k_l + \frac{\mu_t C_{pm}}{Pr_t}, \end{aligned}$$

$$\begin{aligned} \mu_t = c_\mu f_\mu \rho \frac{\kappa^2}{e}, \quad c_\mu = 0.09, \quad f_\mu = \left[ 1 - \exp \left( \alpha_1 R_\kappa \right. \right. \\ \left. \left. + \alpha_3 R_\kappa^3 + \alpha_5 R_\kappa^5 \right) \right]^{1.2}, \end{aligned}$$

$$\begin{aligned} \alpha_1 = -1.5 \times 10^{-4}, \quad \alpha_3 = -1.0 \times 10^{-9}, \quad \alpha_5 = -5.0 \times 10^{-10}, \\ \times R_\kappa = \frac{\kappa^{1/2} y_n}{\nu}, \end{aligned}$$

where  $y_n$  in the expression of  $R_\kappa$  is the normal distance away from the wall,  $k_l$  is the molecular thermal conductivity,  $C_{pm}$

is the specific heat of the gas mixture and  $Pr_t$  is the turbulent Prandtl number.

The vector  $H_l$  in Eq. (1) represents the source term that accounts for the interactions between the gas and liquid phases. In vector  $H_l$ ,  $n_p$  is the number of droplets in the  $p$ th characteristic group of droplets;  $\dot{m}_p$  is the evaporation rate of each particle group;  $\rho_p$  is the liquid density;  $r_p$  is the droplet radius;  $u_p$  and  $v_p$  are the particle velocities at the  $p$ th group;  $h_{fp}$  is the enthalpy of fuel vapor at the droplet surface and  $h\Delta T$  is the convective heat transfer between two phases. Detailed discussions about the liquid phase equations will be described later. The temperature and pressure are calculated iteratively from the following equations

$$\begin{aligned} e = \sum_{i=1}^N Y_i h_i - \frac{p}{\rho}, \quad h_i = h_i'' + \int_{T_{ref}}^T C_{pi} dT, \\ \times p = \rho R_u T \sum_{i=1}^N \frac{Y_i}{W_i}, \end{aligned} \quad (2)$$

where  $R_u$  and  $T_{ref}$  are the universal gas constant and reference temperature for thermodynamic properties, and  $W_i$ ,  $C_{pi}$ ,  $h_i$ ,  $h_i''$  are the molecular weight, constant pressure specific heat, thermodynamic enthalpy, and heat of formation of species  $i$ , respectively.

In reacting flow calculations, the evaluation of thermophysical properties is of vital importance. In this paper, the values of  $C_{pi}$ ,  $k_{li}$  and  $\mu_{li}$  for each species are determined by fourth-order polynomials of temperature, as described in Shuen (Ref. 36). The specific heat of the gas mixture is obtained by mass concentration weighting of individual species. The thermal conductivity and viscosity of the mixture, however, are calculated using Wilke's mixing rule (Ref. 37). The binary mass diffusivity  $D_{ij}$  between species  $i$  and  $j$  is obtained using the Chapman-Enskog theory (Ref. 37).

### C.1a(2) All-Mach-Number Formulation

As noted earlier in the introduction section, the two main difficulties that render the compressible flow algorithms ineffective at low Mach numbers are the roundoff error caused by the singular pressure gradient term in the momentum equations (the pressure term is of order  $1/M^2$  while the convective term is of order unity in the nondimensional momentum equations) and the stiffness caused by the wide disparities in eigenvalues. To circumvent these two problems regarding the low Mach number calculations, following the approach by Merkle and Choi (Ref. 25), Shuen et al. (Ref. 13) added a time preconditioning term to rescale the system eigenvalues and decompose the pressure variable into a constant reference pressure part and a gauge pressure part. This all-Mach-number formulation has been extended to include the turbulent and spray equations. The resulting Navier-Stokes equations in a conservative form are

$$\Gamma \frac{\partial \bar{Q}}{\partial \tau^*} + \frac{\partial \bar{Q}}{\partial \tau} + \frac{\partial (\bar{E} - \bar{E}_c)}{\partial \xi} + \frac{\partial (\bar{F} - \bar{F}_c)}{\partial \eta} = \bar{H}_c + \bar{H}_l, \quad (3)$$

where the primitive variable vector  $\bar{Q}$  and the preconditioned matrix  $\Gamma$  are given as

$$\mathbf{Q} = \frac{1}{J} \begin{pmatrix} p_g \\ u \\ v \\ h \\ \kappa \\ e \\ Y_1 \\ Y_2 \\ \vdots \\ Y_{N-1} \end{pmatrix}, \quad \mathbf{\Gamma} = \begin{bmatrix} 1/\beta & 0 & 0 & 0 & 0 & 0 & \dots & 0 \\ u/\beta & \rho & 0 & 0 & 0 & 0 & \dots & 0 \\ v/\beta & 0 & \rho & 0 & 0 & 0 & \dots & 0 \\ h/\beta - 1 & \rho u & \rho v & \rho & 0 & 0 & \dots & 0 \\ \kappa/\beta & 0 & 0 & \dots & \rho & \dots & 0 & 0 \\ e/\beta & 0 & 0 & \dots & \rho & \dots & 0 & 0 \\ Y_1/\beta & 0 & 0 & 0 & \dots & \rho & \dots & 0 \\ Y_2/\beta & 0 & 0 & 0 & 0 & \dots & \rho & \dots & 0 \\ \vdots & \vdots & \vdots & \vdots & \vdots & \vdots & \vdots & \vdots & \vdots \\ Y_{N-1}/\beta & 0 & 0 & \dots & 0 & \dots & 0 & \dots & \rho \end{bmatrix}$$

where  $\tau^*$  is the pseudotime,  $\beta$  is a parameter for rescaling the eigenvalues of the new system of equations; and  $h = e + p/\rho$  is the specific enthalpy of the gas mixture. The definition of vectors in Eq. (3) is identical to those in Eq. (1) except that the pressure terms in the momentum equations are replaced by gauge pressure,  $p_g$ . The derivation of the all-Mach-number formulation can be found in detail in Shuen et al (Refs. 13 and 14).

### C.1b. Liquid-Phase Equations

#### C.1b(1) Droplet Motion Equations

The liquid phase is treated by solving Lagrangian equations of motion and transport for the life histories of a statistically significant sample of individual droplets. This involves dividing the droplets into  $n$  groups (defined by position, velocity, temperature and diameter) at the fuel nozzle exit and then computing their subsequent trajectories in the flow. The spray model used in this study is based on a dilute spray assumption which is valid in the regions of spray where the droplet loading is low (Refs. 17 and 33). The liquid fuel is assumed to enter the combustor as a fully atomized spray comprised of spherical droplets. The present model does not account for the effects due to droplet breakup and coalescence processes which might be significant in a dense spray situation. The Lagrangian equations governing the droplet motion are

$$\frac{dx_p}{dt} = u_p, \quad (4)$$

$$\frac{dy_p}{dt} = v_p, \quad (5)$$

$$\frac{du_p}{dt} = \frac{3}{16} \frac{C_D \mu_g Re_p}{\rho_p r_p^2} (u_g - u_p), \quad (6)$$

$$\frac{dv_p}{dt} = \frac{3}{16} \frac{C_D \mu_g Re_p}{\rho_p r_p^2} (v_g - v_p). \quad (7)$$

where the particle Reynolds number,  $Re_p$ , and the drag coefficient,  $C_D$ , are defined as

$$Re_p = 2 \frac{r_p \rho_g}{\mu_g} \left[ (u_g - u_p)^2 + (v_g - v_p)^2 \right]^{1/2},$$

$$C_D = \begin{cases} \frac{24}{Re_p} \left( 1 + \frac{Re_p^{2/3}}{6} \right) & \text{for } Re_p < 1000, \\ 0.44 & \text{for } Re_p > 1000. \end{cases}$$

The subscript  $g$  represents the gas-phase quantities and  $p$  represents the liquid-phase (or "particle") quantities. Equations (4) and (5) are used to calculate the new droplet positions and Eqs. (6) and (7) are used to update the new droplet velocities at the new droplet locations. A second-order Runge-Kutta scheme was used to integrate Eqs. (4) to (7).

#### C.1b(2) Droplet Mass and Heat Transfer Equations

As described by Faeth (Ref. 26), the following correlations were used to approximate the mass and heat transfer coefficients for a single isolated spherical droplet:

$$\frac{\dot{m}_p'' d_p}{\rho D_f} = 2 N_s \ln(1 + B), \quad (8)$$

$$\frac{h d_p}{k} = \frac{2 N_p \ln(1 + B) Le^{-1}}{[(1 + B) Le^{-1} - 1]}, \quad (9)$$

where  $h$  is the heat transfer coefficient,  $d_p$  is the droplet diameter,  $D_f$  is the fuel mass diffusivity,  $k$  is the thermal conductivity of fuel vapor and  $\dot{m}_p''$  is the fuel mass evaporation rate per unit area. The  $N_s$  and  $N_p$  are defined as

$$N_s = 1 + \frac{0.276 Re_p^{1/2} Pr^{1/3}}{\left[ 1 + \frac{1.232}{Re_p Pr^{4/3}} \right]^{1/2}},$$

and

$$N_p = 1 + \frac{0.276 Re_p^{1/2} Sc^{1/3}}{\left[ 1 + \frac{1.232}{Re_p Sc^{4/3}} \right]^{1/2}},$$

where  $Sc$  and  $Le$  are the Schmidt and Lewis numbers, respectively. The Spalding number,  $B$ , in Eqs. (8) and (9) is defined as

$$B = \frac{Y_{fgp} - \bar{Y}_{fg}}{1 - Y_{fgp}} \quad (10)$$

where  $Y_{fgp}$  is the fuel vapor mass fraction at the surface of the droplet and  $\bar{Y}_{fg}$  is the mean fuel mass fraction of the ambient gas. In the present study,  $Y_{fgp}$  is obtained from the following equation

$$Y_{fgp} = \frac{X_{fgp} W_f}{X_{fgp} W_f + (1 - X_{fgp}) W_a}, \quad (11)$$

where  $W_a$  is the molecular weight of gas excluding fuel vapor,  $W_f$  is the molecular weight of fuel and  $X_{f,RP}$  is the mole fraction of fuel. The  $X_{f,RP}$  is obtained from the assumption of Raoult's Law. Based on this assumption, the mole fraction at the droplet surface is equal to the ratio of the partial pressure of fuel vapor to the total pressure. For the present spray calculation, the partial pressure of fuel vapor was computed based on the following empirical correlation (Ref. 37):

$$\ln \left( \frac{p_{vp}}{p_c} \right) = \frac{1}{1-x} \left[ p_{v1}x + p_{v2}x^{1.5} + p_{v3}x^3 + p_{v4}x^6 \right] \quad (12)$$

where  $x = 1 - T/T_c$ ,  $p_{v1} = -7.28936$ ,  $p_{v2} = 1.53679$ ,  $p_{v3} = -3.08367$ ,  $p_{v4} = -1.02456$ ,  $T_c$  and  $p_c$  are the critical temperature and critical pressure of the fuel vapor, respectively.

### C.1b(3) Droplet Internal Temperature Equations

As a single droplet enters a hot environment, the immediate small portion of the droplet near the surface will be heating up quickly while the center core of the droplet remains "cold". The heat will be conducted and convected to the entire interior as the droplet penetrates further into the hot ambient gas. Eventually, the temperature within the droplet will become nearly uniform before the end of its lifetime. To solve this transient phenomena within the droplet is not trivial. In the past, certain approximations (Ref. 38) are usually made to alleviate this computational burden while obtaining reasonably good results. Among them, the simplest one is the uniform temperature model. This model assumes that the thermal conductivity of the fuel is infinite. Of course, this is not valid at the beginning of the heating-up process of the droplet. Another model considers the heat diffusion inside the droplet. This yields a conduction model. The temperature distribution within the droplet is obtained by solving the one-dimensional heat conduction equation subject to the convective boundary conditions at the droplet surface. The conduction model completely neglects the convective phenomena within the droplet which might occur due to significant shear forces at the surface induced by high slip velocities. Tong and Sirignano (Ref. 39) developed a *vortex model* for the internal temperature of a single droplet which accounts for the convective effect of the Hill's vortex formation inside the droplet. In this study, Tong and Sirignano's vortex model is applied to obtain the internal temperature distribution of the droplet. The equation governing the internal temperature distribution based on this model is

$$\frac{\partial T_p}{\partial t} = 17 \frac{k_l}{C_{pl}\rho_f r_p^2} \left[ \alpha \frac{\partial^2 T_p}{\partial \alpha^2} + (1 + C(t)\alpha) \frac{\partial T_p}{\partial \alpha} \right] \quad (13)$$

and

$$C(t) = \frac{3}{17} \left( \frac{C_{pl}\rho_l}{k_l} \right) r_p \frac{dr_p}{dt}$$

where the value of  $\alpha$  is between 0 and 1 with  $\alpha = 0$  referring to the vortex center and  $\alpha = 1$  referring to the droplet surface. The initial and boundary conditions for Eq. (13) are

$$\begin{aligned} t &= t_{inj}, \quad T_p = T_{inj}, \\ \alpha &= 0, \quad \frac{\partial T_p}{\partial \alpha} = \frac{1}{17} \left( \frac{C_{pl}\rho_l}{k_l} \right) r_p^2 \frac{\partial T_p}{\partial t}, \\ \alpha &= 1, \quad \frac{\partial T_p}{\partial \alpha} = \frac{3}{16} r_p \frac{\partial T_p}{\partial r} \Big|_s \end{aligned}$$

where  $\frac{\partial T_p}{\partial r} \Big|_s$  is obtained from the energy balance at the droplet surface by the following equation

$$\frac{\partial T_p}{\partial r} \Big|_s = \frac{1}{k_l} \left[ h \Delta T - \dot{m}_p'' h_{fg} \right] \quad (14)$$

where  $\dot{m}_p''$  and  $h$  are calculated from Eqs. (8) and (9), respectively.  $h_{fg}$  is the latent heat of the fuel and  $\Delta T = \bar{T}_g - T_{p,s}$ , where  $T_{p,s}$  is droplet surface temperature and  $\bar{T}_g$  is the mean gas temperature evaluated in the following way

$$\bar{T}_g = \frac{1}{3} T_g + \frac{2}{3} T_{p,s}$$

An implicit scheme was used to solve Eq. (13) subject to the initial and boundary conditions. Second-order central differences were used for the spatial differential terms and a first-order difference for the time term. These treatments rendered a scalar tridiagonal algebraic system and was solved by the Thomas algorithm (Ref. 40).

## C.2 NUMERICAL METHODS

### C.2a Discretized Equations

Equation (3) is the final gas-phase governing equation to be solved numerically. To obtain time-accurate solutions for time-evolving problems, a dual time-stepping integration method can be applied to Eq. (3). The solution converged in pseudotime corresponds to a time-accurate solution in physical time (Ref. 13). However, for the present study, since only the steady state solution is of our interest, the physical time term in Eq. (3) can be dropped and the solution can be marched completely in pseudotime to obtain the final steady state solution. One advantage of marching to the steady state solution in pseudotime is that the convergence of the marching (iterative) process is determined by the eigenvalue characteristics on the pseudotime space and not by the original stiff eigenvalues. The analysis of the eigensystem has been performed in our previous study (Refs. 13 and 14) and therefore will not be repeated here. It should be noted that the inclusion of the turbulent  $\kappa$ - $\epsilon$  equations in this study does not affect the system eigenvalues at all and, therefore, the properties of the all-Mach-number formulation analysis in previous papers (Refs. 13 and 14) are still valid.

After linearization and applying a first-order time differencing, Eq. (3) can be expressed in the following form:

$$\begin{aligned} & \left[ \Gamma - \Delta \tau^* D + \Delta \tau^* \left( \frac{\partial A}{\partial \xi} - \frac{\partial}{\partial \xi} R_{\xi\xi} \frac{\partial}{\partial \xi} \right) \right. \\ & \quad \left. + \Delta \tau^* \left( \frac{\partial B}{\partial \eta} - \frac{\partial}{\partial \eta} R_{\eta\eta} \frac{\partial}{\partial \eta} \right) \right]^p \\ & \quad \times \Delta \hat{Q} = -\Delta \tau^* (R)^p, \end{aligned} \quad (15)$$

where

$$R^p = \frac{\partial(\tilde{E} - \tilde{E}_v)^p}{\partial \xi} + \frac{\partial(\tilde{F} - \tilde{F}_v)^p}{\partial \eta} - \tilde{H}_c^p - \tilde{H}_l^p, \quad (16)$$

where  $p$  denotes the previous iteration level,  $D$  is the Jacobian for chemical and turbulent source terms,  $A$  and  $B$  are the inviscid term Jacobians and  $R_{\xi\xi}$  and  $R_{\eta\eta}$  are the viscous term Jacobians. The expressions for these Jacobians can be found in Shuen et al. (Refs. 13 and 14) except for the turbulent part. Central differences were used to discretize the spatial derivative terms in Eqs. (15) and (16) for both explicit and implicit operators. The resulting coupled algebraic equations are solved using a modified strongly implicit procedure (MSIP) proposed by Schneider and Zedan (Ref. 41), which is completely vectorizable along  $i + 2j$  diagonal direction.

### C.2b Boundary Conditions

The boundary conditions for gas phase equations are described as follows. Here, only the subsonic flow boundary conditions are considered in the present paper. At the inlet, all quantities are specified except pressure which is obtained through extrapolation from the pressure at interior points. At the exit, the governing equations are solved at the exit station by applying backward differences for the streamwise derivative terms (central differences are still used for cross-stream derivative terms). However, the streamwise pressure derivative terms are *centrally-differenced*. This treatment requires the pressure information at the station one step downstream (outside the computational domain) where a constant pressure condition is enforced. At the symmetry line, the governing equations are solved via the use of the symmetry conditions for two-dimensional flows. For the axisymmetric case, a singularity exists at this line and a simple one-sided difference is used to implement the symmetry conditions. At the solid wall, no slip conditions are used for the velocities and an adiabatic wall is assumed. Normal derivatives for species,  $Y_i$ , and  $(\rho_r + 2/3 \rho \kappa)$  are set to zero. For the turbulent quantities, the low Reynolds number turbulence model (Ref. 35) used in this study requires the specification of the  $\kappa$  and  $\epsilon$  at the walls as follows:

$$\begin{aligned} \kappa &= 0.250 u_\tau^2 \\ \epsilon &= 0.251 \frac{u_\tau^4}{\nu} \end{aligned}$$

where  $u_\tau$  is the friction velocity at the wall.

Since a multiblock treatment is applied to the present numerical algorithm, the interfaces between blocks (or zones) become a special kind of boundary. At the interface, the governing equations are still solved without any distinction from the rest of the interior points. The flow variables have been carefully arranged in such a way that the information from the neighboring block(s) is automatically brought into the calculation at the interface of the current block. The multiblock treatment of the present study not only provides flexibility for complex geometry calculations but also reduces the size of the storage array for the MSIP coefficients due to the smaller sizes of the subdomains.

### C.2c Spray Source Terms

In Eq. (3), the liquid-phase interaction with the Navier-Stokes equations is modeled as a source term which accounts for mass, momentum and energy exchanges between two phases. In order to compute this source term, the liquid-phase governing equations described in the previous section are integrated in time once initial conditions have been specified. As a liquid droplet begins its journey from the injection nozzle, its position, velocity, temperature and size, in general, will be changing according to the interaction between the gas-phase solution and the spray properties. In contrast to the Eulerian approach for the gas-phase equations, the Lagrangian treatment for the liquid-phase equations requires interpolation of the flow quantities from the Eulerian grid to the particle positions and redistribution of the spray source terms from the particle positions to the Eulerian grid for the gas-phase. Since the time step for the spray equations is usually much smaller than that for the flow equations (especially for the present MSIP scheme with which, in general, a large CFL number can be obtained) and a large number of particle groups are required to statistically represent the spray behavior, it is very important to keep the numerical efficiency of the present implicit scheme from being severely degraded down by the coupling (or inter-action) between the gas and liquid-phases. A strategy to overcome this problem, at least for steady state flows, has been successfully applied to the present study. It will be described in this section.

#### C.2c(1) Stochastic Process

As mentioned in the introduction section, there are two types of separated flow models for spray computations. One is the deterministic separated flow (DSF) model and the other the stochastic separated flow (SSF) model. For turbulent flow calculations, the DSF model completely neglects the dispersion effect due to the turbulent motion and, therefore, mean gas flow quantities are used to evaluate the right-hand-side of Eqs. (6) and (7). In the present study, the SSF model is applied to account for the dispersion effects on spray characteristics. In this model, the gas-phase velocity fluctuations,  $u'_i$  and  $v'_i$ , are generated by randomly sampling a Gaussian probability density distribution having a standard deviation of  $(2\kappa/3)^{1/2}$ . The instantaneous velocities are then used to evaluate Eqs. (6) and (7). A fixed number of samplings is conducted for each group of particles. The final spray quantities are obtained by averaging the results (source terms, trajectories, . . . , etc.) among the total samples. Details of the SSF model can be found in Refs. 26 and 33.

### C.2c(2) Determination of Spray Time Step

For spray combustion calculations, there are several time scales involved in the flow field which can differ by several orders of magnitude. The chemical reaction time scale is usually very small compared with the rate of evolution of the gas flow. This is also true for an evaporating spray. To accurately calculate the particle trajectories, size and temperature, the integration time step has to be small. This is especially severe as the droplet becomes smaller and smaller toward the end of its lifetime. For an unsteady problem, the time step for the entire system will be controlled by the smallest time step. For a steady state calculation, however, the time step for chemical reaction is usually not a problem in the present formulation due to the implicit treatment of the chemical source term. Our experience indicates that, for single-phase combustion calculations, the same CFL number usually can be used for both nonreacting and reacting calculations with the present MSIP method. This ensures that the convergence properties for reacting flow calculations are not degraded using the present numerical algorithm. However, the time step for spray equations still remains small and has to be selected (computed) very carefully in order to obtain accurate spray results and to maintain stability. The determination of the spray time step will be discussed here and how the spray interacts with the gas flow is described in the next section.

The spray time step at any instant of time along its trajectory is determined based on the following time step constraints: (1) droplet velocity relaxation time ( $t_r$ ), (2) droplet life time ( $t_l$ ), (3) droplet surface temperature constraint time ( $t_s$ ), (4) local grid time scale ( $t_g$ ) and (5) turbulent eddy-droplet interaction time ( $t_i$ ). The final spray time step ( $\Delta t_{spr}$ ) is determined by taking the minimum of the above five time steps to ensure the accuracy and stability of the spray calculations. A factor between 0.1 and 0.5 is further used to multiply the selected time step in the current spray calculation. These time steps are described as follows.

**Droplet velocity relaxation time ( $t_r$ ):** The local linearized droplet equations of motion, Eqs. (6) and (7), have exact solutions in terms of the local slip velocity with an exponential decay form. The time constant for the exact solution can be expressed as

$$t_r = \frac{16}{3} \left( \frac{\rho_l}{\rho_g} \right) \left( \frac{r_p^2}{\nu} \right) (C_D Re_p)^{-1}.$$

**Droplet life time ( $t_l$ ):** To ensure that the drop size remains positive for the practical computational purpose, the droplet lifetime at any instant of time is estimated by the following equation

$$t_l = \frac{r_p}{3\dot{m}_p \rho_l}.$$

**Droplet surface temperature constraint time ( $t_s$ ):** When the governing equation for the droplet internal temperature distribution, Eq. (13), is solved, the temperature solution can become completely incorrect due to the use of an inappropriately large time step. This is particularly important for fuel with a low boiling temperature (close to room temperature).

In order to ensure the success of the temperature calculation using Eq. (13), the exact solution of the infinite conductivity model (or uniform temperature model) is used to estimate the time step for the present vortex model. The temperature equation for the droplet based on this model is

$$\frac{dT_p}{dt} = \frac{6}{\rho_l C_{v,p}} \left[ h(\bar{T} - T_p) - \dot{m}_p'' h_{fg} \right] \quad (17)$$

Equation (17) has an exact solution (after local linearization) in the following form

$$\Delta T_p = A(1 - e^{-A't}).$$

where  $\Delta T_p$  is the droplet temperature change within the integration time step.  $A$ ,  $A'$ , and  $B'$  are defined as

$$A = \left( \bar{T} - T_p - \frac{B'}{A'} \right),$$

$$A' = \frac{6}{\rho_l C_{v,p}} h,$$

$$B' = \frac{6}{\rho_l C_{v,p}} \dot{m}_p'' h_{fg}.$$

Therefore, a time scale can be obtained based on the above solution if a desired  $\Delta T_p$  is specified. This time scale is expressed as

$$t_s = \ln \left( \frac{1}{1 - \frac{\Delta T_p}{A}} \right) / A'$$

In our spray calculation,  $\Delta T_p = 3 \text{ K}$  is specified for those particles just leaving the injector, where they experience a sudden temperature jump and  $\Delta T_p = 0.5 \text{ K}$  for the rest of the calculation toward the end of their lifetime.

**Local grid time scale ( $t_g$ ):** A particle can travel across several grids and may experience a sudden change of the local gas properties if the time step is too large. This not only causes inaccuracy in the integration but also increases the difficulties of locating the particle positions. Therefore, a time scale,  $t_g$ , is computed to ensure that the particle only moves less than one local cell size in one time step.

**Turbulent Eddy-droplet interaction time ( $t_i$ ):** According to Shuen et al. (Ref. 42), a particle is assumed to interact with an eddy for a time which is the minimum of either the eddy lifetime or the transit time required for the particle to cross the eddy. These times are estimated by assuming that the characteristic size of an eddy is the dissipation length scale as

$$L_e = C_\mu^{3/4} \kappa^{3/2} / \epsilon$$

and the eddy lifetime is estimated as

$$t_e = L_e / (2 \kappa / 3)^{1/2}.$$

The transit time of a particle was found using the linearized equation of motion for a particle in a uniform flow

$$t_i = -\tau \ln \left[ 1 - L_e \left( \tau |\vec{u}'' - \vec{u}_p''| \right) \right] \quad (18)$$

where

$$\tau = \frac{8\rho_f r_p}{3\rho_g C_D |\vec{u}'' - \vec{u}_p|}$$

and  $\vec{u}'' - \vec{u}_p$  is the relative velocity at the start of the interaction. When  $L_e > \tau |\vec{u}'' - \vec{u}_p|$ , the linearized stopping

distance of the particle is smaller than the characteristic length scale of the eddy and Eq. (18) has no solution. In this case, the eddy has captured the particle and the interaction time is the eddy lifetime. Therefore

$$t_i = t_e \quad \text{if } L_e > \tau |\vec{u}'' - \vec{u}_p|$$

$$t_i = \min(t_e, t_f) \quad \text{if } L_e < \tau |\vec{u}'' - \vec{u}_p|$$

### C.2c(3) Interaction Between Two Phases

For the gas-phase equations, Eq. (3), the presence of the spray appears in the form of a source term,  $H_f$ . This source term represents the interchange of the mass, momentum and energy between two phases. As the particles are injected into the flow domain, their subsequent behavior (positions, velocities, size, and temperature) is affected continuously by the neighboring gas properties and *vice versa*. Usually a large number of spray particles is desirable to accurately predict the spray behavior. However, this requires tremendous computational effort for the spray calculation alone. To minimize the computational time for the spray, the spray source term,  $H_f$ , is not required to be updated at every gas-phase iteration (pseudotime time marching). Usually the spray source term is updated every 10 to 20 iterations in our spray calculations. When the spray source term is updated, each group of particles is integrated either to the end of its lifetime or until it leaves the computational domain. It should be noted that, for the present steady state spray combustion calculation, the spray time step determined previously is independent of the pseudotime used for the gas-phase equations, which is determined mainly from the obtainable maximum CFL number according to the local system eigenvalues. Therefore, this strategy maintains both the efficiency of the flow solver and the accuracy of the spray Lagrangian integration. This treatment of the gas-liquid interaction is different from those reported by Raju and Sirignano (Ref. 17) where time-accurate solutions were their primary concern. In the present computation, it is assumed that upon impingement with the walls, the droplets evaporate completely and assume the local gas flow velocities. The interpolation of the gas-phase properties from the Eulerian grid to the particle location and the redistribution of the spray source term from the particle location to the Eulerian grid is applied in a similar way as discussed in Raju and Sirignano (Ref. 17).

## C.3 NUMERICAL TEST RESULTS

In this section, results obtained from the ALLSPD algorithm with and without spray are presented. These include (1) a nonreacting turbulent backward-facing step flow to demonstrate the validity of the current turbulence model, (2) a single-phase turbulent reverse jet combustion flow to assess the present combustion treatment and (3) a spray gas turbine

combustion flow to qualitatively demonstrate the spray calculation for a complex geometry and the interaction between the two phases. The spray results shown here emphasize the numerical aspect rather than the spray physics. The accuracy validation for spray calculations will be considered in future calculations.

### C.3a Backward-Facing Step Flow

The turbulent backward-facing step flow data of Kim et al. (Ref. 43) for a two-dimensional channel with an inlet to step height ratio of two is selected here to test the validity of the  $\kappa$ - $\epsilon$  turbulence model. A  $136 \times 100$  grid, clustered near the step and the top and bottom walls, was used. No chemical reactions were included in the calculation.

The particle traces of the flow is shown in Fig. 8. The experimental reattachment length given by Kim et al. is  $7.1 H$ , where  $H$  is the step height. The predicted value in our calculation is about  $6.1 H$ , which represents a 14 percent underprediction. Figure 9 shows the mean velocity profiles at various axial locations. The agreement is quite good in all locations except near the reattachment point. The profiles for the turbulent kinetic energy and turbulent shear stress are given in Fig. 10. Good agreement is observed in these comparisons. Wall pressure coefficients along the step-side and opposite walls are shown in Fig. 11. The underprediction of reattachment length is also evident from this figure. The predicted pressure recovery downstream of the reattachment point is in excellent agreement with measured pressure levels. The convergence history for this calculation is illustrated in Fig. 12. The convergence property for the calculation is satisfactory.

### C.3b Reverse Jet Combustion Flow

The flow configuration is a 51 mm I.D. (inner diam) times 457 mm cylindrical chamber containing a reverse jet flame holder which issues from a 1.32 mm I.D. (6.35 mm O.D.) tube. The jet is coincident with the chamber axis and located 80 mm upstream from the chamber exit. Both the main and jet flows are stoichiometrically premixed propane and air at a temperature of 300 K, with a mean velocity of 7.5 m/s for the main stream and 135 m/s for the jet. A complete description of the flow system is available in McDannel et al. (Ref. 44). A  $117 \times 61$  grid (half domain) clustered near the jet tube was used. Five species ( $C_3H_8$ ,  $O_2$ ,  $N_2$ ,  $CO_2$ , and  $H_2O$ ) were considered in this calculation and the single-step global reaction chemistry model reported in Westbrook and Dryer (Ref. 45) was used for combustion. Figures 13, 14, and 15 show the particle traces, velocity vectors (colored by temperature) and temperature contours of the reacting flow, respectively. The experimentally measured temperature contours (directly taken from McDannel et al. (Ref. 44)) are also presented in Fig. 15 for comparison. The flow is clearly seen to consist of two distinct regions - the recirculation zone and the wake. The incoming flow is ignited by the hot combustion gas in the recirculation zone and further combustion takes place in the wake. For the test conditions considered here the reverse jet serves as a very effective flame holding device. The results in Fig. 15 indicate that the predicted temperatures are higher than the measured values. This is mainly attributed to the over-simplified chemistry model used in the present calculation. As reported by McDannel et al. (Ref. 44), there

was a significant amount of carbon monoxide (CO) observed in the combustion products, which lowered the combustion temperature. Also not included in the calculation is the radiation heat loss which will lower the flow temperature further. In addition, the thermocouple's used in the measurements were not corrected for radiation loss, indicating that the actual gas temperatures would be somewhat higher than measured.

### C.3c Gas Turbine Spray Combustion Flow

A simplified model of General Electric's EEE (Energy Efficiency Engine) combustor is considered. Figure 16 shows the clustered  $81 \times 65$  grid for this calculation and the general engine grid layout for the entire engine (Ref. 46). It is an annular combustor with a dual can combustor dome. The cooling air through the internal walls (two combustor domes) was omitted for simplicity. Also, the swirling effect was not included in the calculation. The present calculation does not completely simulate the typical gas turbine combustion characteristics, in which swirling and cooling are the two important ingredients. We would like to emphasize, in the present study, that the focus is to demonstrate the effectiveness of the interaction between the two phases based on the present spray solution procedure. Further studies with this algorithm will be conducted both on the spray accuracy evaluation and on the detailed swirling and cooling computation for gas turbine combustor configurations.

For the present spray combustion calculation, the spray injectors were located close to the inlet of the combustor domes. One hundred spray groups with 10 random samples for each group were used, which can be seen in Fig. 17. The case studied here has a flow Reynolds number,  $Re = 1.05 \times 10^5$ , where the Reynolds number is based on the inlet maximum velocity and combustor inlet height. The inlet air temperature is 900 K and the pressure is 1 atm. The liquid n-pentane fuel was used and five species ( $C_5H_{12}$ ,  $O_2$ ,  $N_2$ ,  $CO_2$ , and  $H_2O$ ) were considered in this calculation. Again, the single-step global reaction chemistry model reported in Westbrook and Dryer (Ref. 45) was used for combustion. The fuel/air ratio is 0.02 (total fuel injected/total incoming air at the inlet, including bypass air). The injection velocity of the liquid fuel at the exit of the fuel nozzle is 20 m/s and the temperature is 290 K. The liquid fuel was assumed to be fully atomized with the initial diameters ranging from 20 to 100  $\mu m$ . The liquid fuel was injected into the gas flow after the gas flow had been iterated to reach a nearly steady state solution. Upon the injection of the fuel, the cool fuel was suddenly exposed to a hot environment and the interaction between the two phases took place in terms of the interchange of mass, momentum and energy. An ignition source was placed downstream of the injector to ignite the "burning" of the fuel-air mixture. The ignitor was turned on right after the initiation of the spray and was turned off when the temperature in any of the ignition computational cells reached 1600 K. The spray source term,  $H_1$ , in Eq. (3) was updated (computed) every 20 gas-phase iterations. The converged results are presented in the following figures.

Figure 10 shows the particle trajectories. The dots in the figure are not scaled to indicate the relative size of the actual liquid particles, although smaller particles evaporate much faster than bigger ones. The computed velocity vectors colored

with temperature are presented in Fig. 18, where a converged solution of the cold flow (nonspray/noncombustion) with the same flow condition is also included for comparison. The combustion zones are confined near the inner walls. This is mainly due to the exclusion of the swirlers at the inlet of the combustor domes in the present calculation. Without swirl, the degree of the fuel-air mixing is relatively poor. As may be noted, there is no flame holding device for the present calculation. The recirculation zones near the inner walls are the only devices to hold the flame. Figure 19 shows the Sauter mean diameter,  $D_{32}$ , along the averaged trajectory for both the lower and upper domes. The increase of the  $D_{32}$  right after the injection indicates the rapid evaporation of the smaller particles. After reaching a peak, both mean diameters gradually decrease as more and more particles evaporate. To show the convergence properties for both nonreacting and spray combustion cases, the convergence histories for both cases are shown in Fig. 20. As can be seen in this figure, the spray was initiated after the gas-phase solution had been iterated 1000 times. A sudden disturbance from the spray injection causes the L2 norm residual to jump to a level higher than the initial gas-phase residual. As more and more spray particles evaporate and undergo combustion, the interaction between two phases can be clearly identified in this convergence pattern. Since in the present calculation, the spray source term was updated every 20 gas-phase iterations, a small residual spike along the convergence history can be seen very clearly. These small spikes persist toward the end of the present computation.

### D. CONCLUDING REMARKS

Much work is required to develop a CFD code to the level necessary for a designer to be able to use it with confidence. We at NASA are proceeding with a commitment to do this. A three-dimensional version of our ALLSPD will be developed shortly and extensive validation against experimental data will be performed. At the same time we are exploring the use of advanced modeling to better represent the flow physics and chemistry of turbulent combustion. For example, modeling of dense sprays and sprays at super-critical conditions will be investigated. Modeling of the turbulence and chemistry interaction will be explored, using techniques such as PDF methods. The use of reduced hydrocarbon chemical kinetics models which represent the actual combustion processes are also necessary. And finally, an improved model to represent potentially high levels of radiation heat transfer is also needed.

The state of art for numerics also continues to advance at a rapid pace. Our code will be modified in the future as opportunities arise in areas such as unstructured grids and massively parallel computing. This ongoing effort to produce a modern chemical reacting flow CFD code holds promise to provide a powerful design tool for the industry's use in the analyses of the next generation of gas turbine engine combustor concepts.

### E. REFERENCES

1. Bulzan, D.L., "Velocity and Drop Size Measurements in a Swirl-Stabilized, Combusting Spray," SPIE Paper No. 1862-12, 1993.
2. Chigier, N.A., "Gas Dynamics of Swirling Flow in Combustion Systems," *Astronaut. Acta*, Vol. 17, 1972, pp. 387-395.

3. Syred, N. and Beer, J., "Combustion in Swirling Flows: A Review," Combust. Flame, Vol. 23, 1974, pp. 143-201.
4. Lilley, D.G., "Swirl Flows in Combustion: A Review," AIAA J., Vol. 15, No. 8, 1977, pp. 1063-1078.
5. Styles, A.C. and Chigier, N.A., "Combustion of Air Blast Atomized Spray Flames," Sixteenth Symposium (International) on Combustion, The Combustion Institute, Pittsburgh, PA, 1976, pp. 619-630.
6. Khalil, E.E. and Whitelaw, J.H., "Aerodynamic and Thermodynamic Characteristics of Kerosene-Spray Flames," Sixteenth Symposium (International) on Combustion, The Combustion Institute, Pittsburgh, PA, 1976, pp. 569-576.
7. Bachalo, W.D. and Houser, M.J., "Phase/Doppler Spray Analyzer for Simultaneous Measurements of Drop Size and Velocity Distributions," Opt. Eng., Vol. 23, No. 5, 1984, pp. 583-590.
8. McDonell, V.G. and Samuelsen, S., "Gas and Drop Behavior in Reacting and Non-Reacting Air-Blast Atomizer Sprays," J. Propuls. Power, Vol. 7, No. 5, 1991, pp. 684-691.
9. Zurlo, J.R., Presser, C., Gupta, A., and Semerjian, H.G., "Determination of Droplet Characteristics in Spray Flames Using Three Different Sizing Techniques," AIAA Paper 91-2200, 1991.
10. Edwards, C.F., Rudoff, R.C., and Bachalo, W.D., "Measurement of Correlated Drop Size and Velocity Statistics, Size Distribution, and Volume Flux in a Steady Spray Flame," Presented at the Fifth International Symposium on the Applications of Laser Techniques to Fluid Mechanics, Lisbon, Portugal, 1990.
11. McDonell, V.G. and Samuelsen, G.S., "Application of Two-Component Phase Doppler Interferometry to the Measurement of Particle Size, Mass Flux, and Velocities in Two-Phase Flows," Twenty-Second Symposium (International) on Combustion, The Combustion Institute, Pittsburgh, PA, 1988, pp. 1961-1971.
12. Edwards, C.F. and Rudoff, R.C., "Structure of a Swirl-Stabilized Spray Flame by Imaging, Laser Doppler Velocimetry, and Phase Doppler Anemometry," Twenty Third Symposium (International) on Combustion, The Combustion Institute, Pittsburgh, PA, 1990, pp. 1353-1359.
13. Shuen, J.-S., Chen, K.-H., and Choi, Y., "A Time-Accurate Algorithm for Chemical Non-Equilibrium Viscous Flows at All Speeds," AIAA Paper 92-3639, 1992.
14. Shuen, J.-S., Chen, K.-H., and Choi, Y., "A Coupled Implicit Method for Chemical Non-Equilibrium Flows at All Speeds," Accepted for Publication, J. Comput. Phys., 1993.
15. Solomon, A.S.P., Shuen, J.-S., Zhang, Q.-F., and Faeth, G.M., "Measurements and Predictions of the Structure of Evaporating Sprays," J. Heat Transfer, Vol. 107, 1985, pp. 679-686.
16. Shuen, J.-S., "Prediction of the Structure of Fuel Sprays in Cylindrical Combustion Chambers," J. Propuls. Power, Vol. 3, 1987, pp. 105-113.
17. Raju, M.S. and Sirignano, W.A., "Multicomponent Spray Computations in a Modified Centerbody Combustor," J. Propuls. Power, Vol. 6, 1990, pp. 97-105.
18. Liou, M.-S., "Newton/Upwind Method and Numerical Study of Shock Wave/Boundary Layer Interactions," Int. J. Numer. Methods/Fluids, Vol. 9, 1989, pp. 747-761.
19. Meakin, R. and Suhs, N., "Unsteady Aerodynamic Simulation of Multiple Bodies in a Relative Motion," AIAA Paper 89-1996, 1989.
20. Pan, D. and Chakravarthy, S., "Unified Formulation for Incompressible Flows," AIAA Paper 89-0122, 1989.
21. Chen, K.-H., Kelec, F.J., and Pletcher, R.H., "A Numerical and Experimental Study of Three-Dimensional Liquid Sloshing in a Rotating Spherical Container," AIAA Paper 92-0829, 1992.
22. Shuen, J.-S. and Yoon, S., "Numerical Study of Chemically Reacting Flows Using a Lower-Upper Symmetric Successive Overrelaxation Scheme," AIAA J., Vol. 27, No. 12, 1989, pp. 1752-1760.
23. Merkle, C.L. and Choi, D., "Application of Time-Iterative Schemes to Incompressible Flow," AIAA J., Vol. 23, No. 12, 1985, pp. 1518-1524.
24. Turkel, E., "Preconditioned Methods for Solving the Incompressible and Low Speed Compressible Equations," J. Comput. Phys., Vol. 72, 1987, pp. 277-298.
25. Merkle, C.L. and Choi, Y., "Computation of Low-Speed Flow with Heat Addition," AIAA J., Vol. 25, No. 8, 1987, pp. 831-838.
26. Faeth, G.M., "Evaporation and Combustion of Sprays," Prog. Energy Combust. Sci., Vol. 9, No. 1-2, 1983, pp. 1-76.
27. Sirignano, W.A., "Fuel Droplet Vaporization and Spray Combustion Theory," Prog. Energy Combust. Sci., Vol. 9, No. 4, 1983, pp. 291-322.
28. Shearer, A.J., Tamura, H., and Faeth, G.M., "Evaluation of a Locally Homogeneous Flow Model of Spray Evaporation," J. Energy, Vol. 3, No. 1, 1979, pp. 271-284.
29. Gosman, A.D. and Johns, R.J.R., "Computer Analysis of Fuel-Air Mixing in Direct-Injection Engines," Diesel Combustor and Emission, SEA P-86, SAE, Warrendale, PA, 1980.
30. Crowe, C.T., "Review-Numerical Models for Dilute Gas-Particle Flows," J. Fluids Eng., Vol. 104, No. 3, 1982, pp. 297-303.
31. Dukowicz, J.K., "A Particle-Fluid Numerical Model for Liquid Sprays," J. Comput. Phys., Vol. 35, No. 2, 1990, pp. 229-253.
32. Gosman, A.D. and Ioannides, E., "Aspects of Computer Simulation of Liquid-Fueled Combustors," J. Energy, Vol. 7, No. 6, 1983, pp. 482-490.
33. Shuen, J.-S., Solomon, A.S.P., and Faeth, G.M., "Drop-Turbulence Interactions in a Diffusion Flame," AIAA J., Vol. 24, No. 1, 1986, pp. 101-108.
34. Chen, K.-H. and Shuen, J.-S., "A Coupled Multi-Block Solution Procedure for Spray Combustion in Complex Geometries," AIAA Paper 93-0108, 1993.
35. Shih, T.H., "An Improved  $\kappa$ - $\epsilon$  Model for Near-Wall Turbulence and Comparison with Direct Numerical Simulation," NASA TM-103221, 1990.
36. Shuen, J.-S., "Upwind Differencing and LU Factorization for Chemical Non-equilibrium Navier-Stokes Equations," J. Comput. Phys., Vol. 99, No. 2, 1992, pp. 233-250.

37. Reid, R.C., Prausnitz, J.M., and Poling, B.E., "The Properties of Gases and Liquids, Fourth Ed., McGraw-Hill Publishing Co., New York, 1988.
38. Aggarwal, S.K., Tong, A.Y., and Sirignano, W.A., "A Comparison of Vaporization Models in Spray Calculations," *AIAA J.*, Vol. 22, No. 10, 1984, pp. 1448-1457.
39. Tong, A.Y. and Sirignano, W.A., "Analytical Solution for Diffusion and Circulation in a Vaporizing Droplet," *Nineteenth Symposium (International) on Combustion*, The Combustion Institute, Pittsburgh, PA, 1982, pp. 1007-1020.
40. Anderson, D.A., Tannehill, J.C., and Pletcher, R.H., *Computational Fluid Mechanics and Heat Transfer*, Hemisphere Publishing Corp., New York, 1984.
41. Schneider, G.E. and Zedan, M., "A Modified Strongly Implicit Procedure for the Numerical Solution of Field Problems," *Numer. Heat Transfer*, Vol. 4, No. 1, 1981, pp. 1-19.
42. Shuen, J.-S., Chen, L.D., and Faeth, G.M., "Evaluation of a Stochastic Model of Particle Dispersion in a Turbulent Round Jet," *AIChE J.*, Vol. 29, No. 1, 1983, pp. 167-170.
43. Kim, J., Kline, S.J., and Johnston, J.P., "Investigation of a Reattaching Turbulent Shear Layer: Flow Over a Backward-Facing Step," *J. Fluids Eng.*, Vol. 102, No. 3, 1980, pp. 302-308.
44. McDannel, M.D., Peterson, P.R., and Samuelsen, G.S., "Species Concentration and Temperature Measurements in a Lean, Premixed Flow Stabilized by a Reverse Jet," *Combust. Sci. Technol.*, Vol. 28, No. 5-6, 1982, pp. 211-224.
45. Westbrook, C.K. and Dryer, F.L., "Simplified Reaction Mechanisms for the Oxidation of Hydrocarbon Fuels in Flames," *Combust. Sci. Technol.*, Vol. 27, No. 1-2, 1981, pp. 31-43.
46. Stewart, M.E.M., "Euler Solutions of an Unbladed Jet Engine Configuration," NASA TN-105332, 1991.

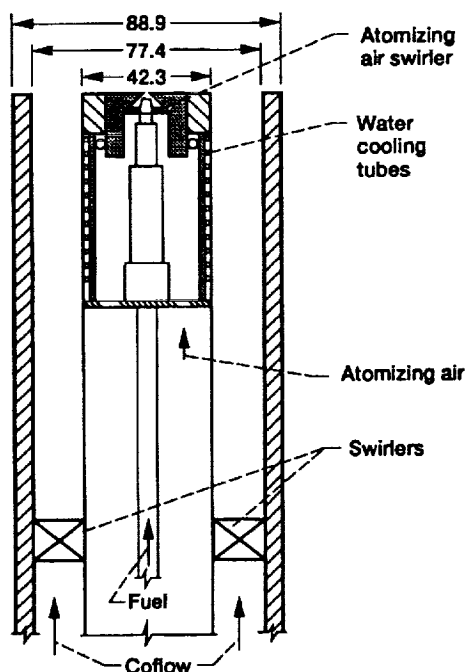


Figure 1.—Schematic drawing of the combustor. Dimensions in mm.

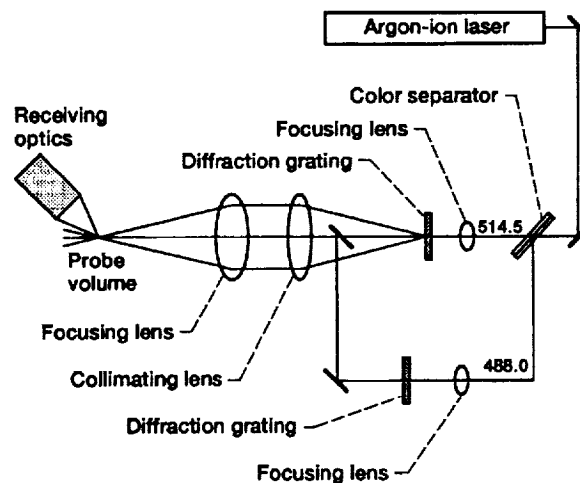


Figure 2.—Optical configuration of the phase/Doppler particle analyzer.

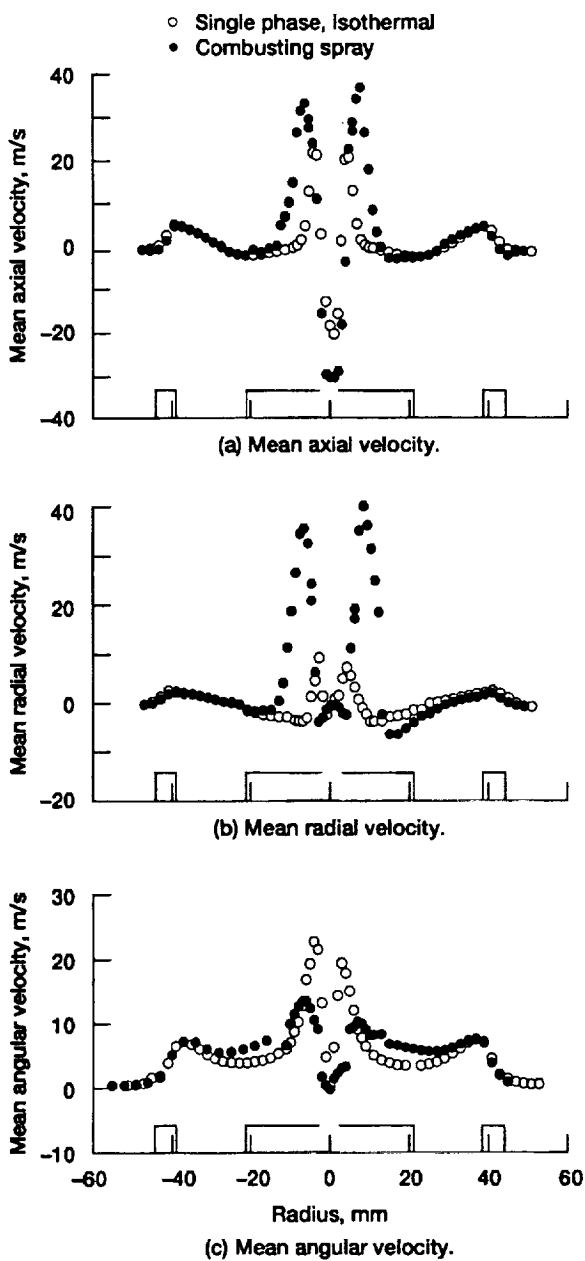


Figure 3.—Gas phase mean velocity at 5 mm downstream.

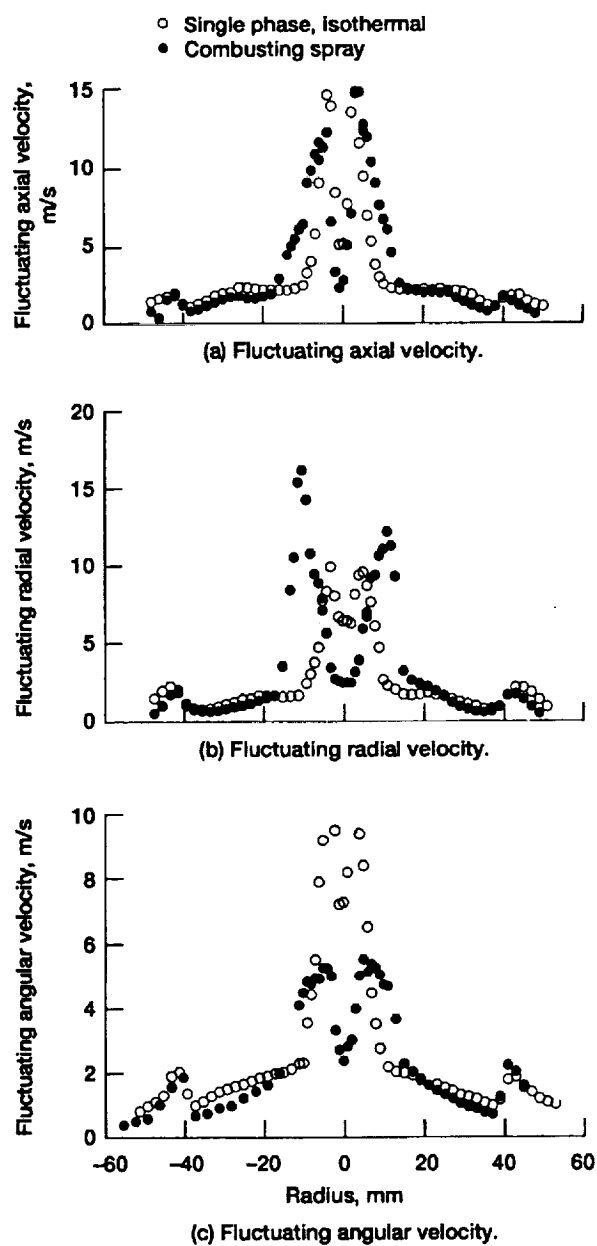


Figure 4.—Gas phase fluctuating velocity at 5 mm downstream.

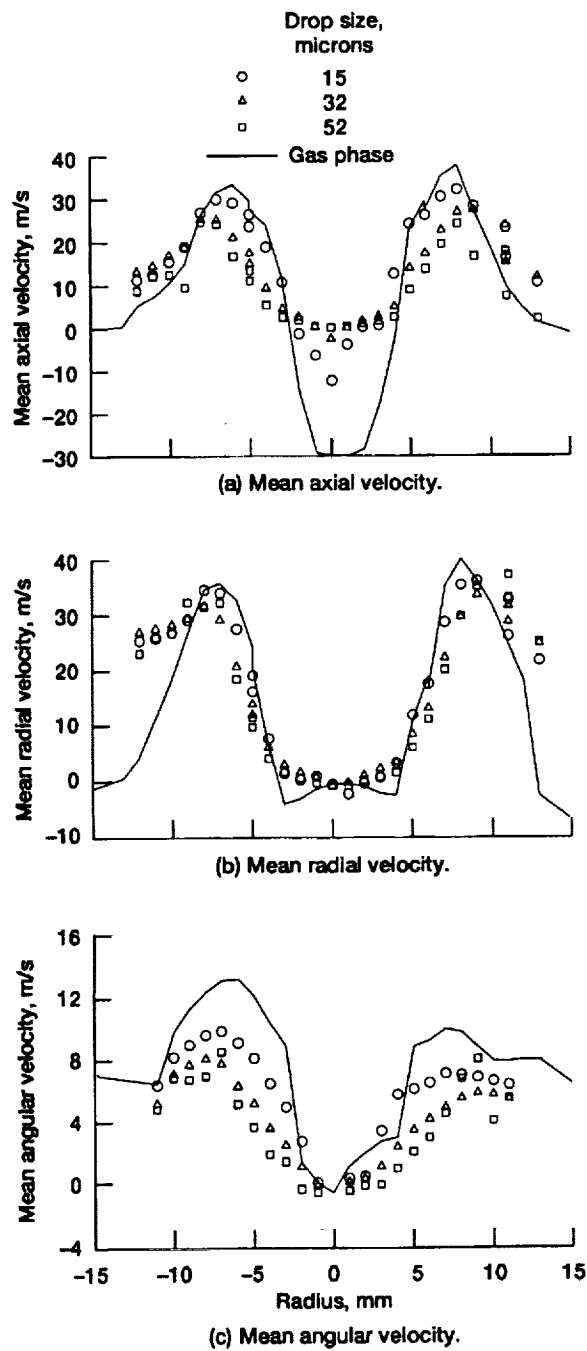


Figure 5.—Drop mean velocity at 5 mm downstream.

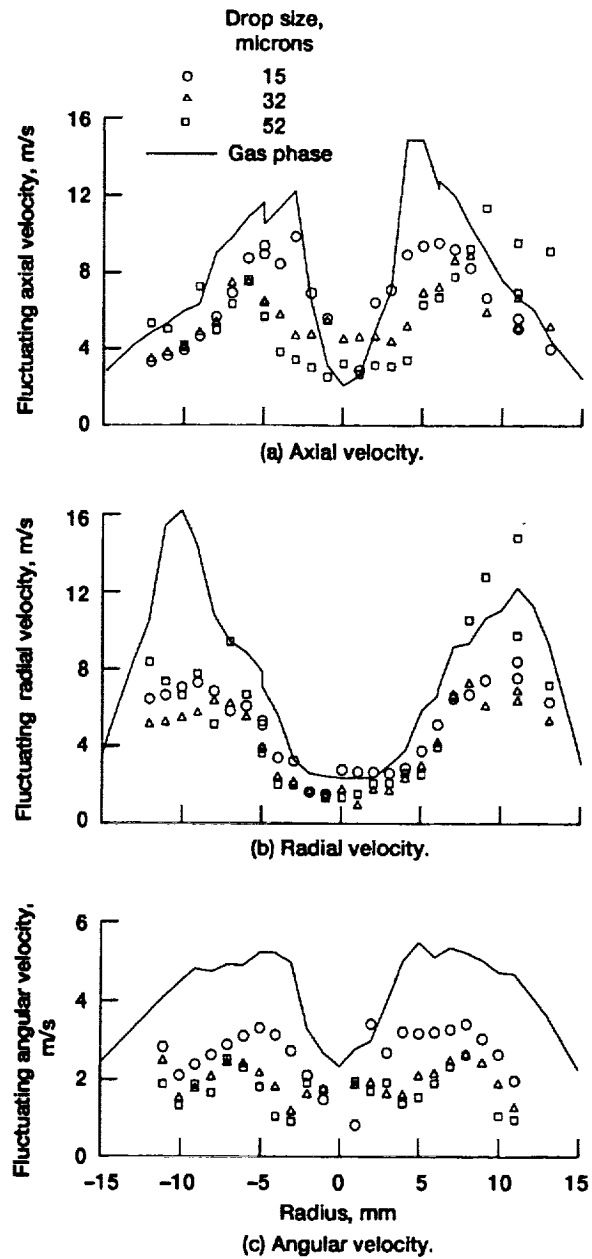


Figure 6.—Drop fluctuating velocity at 5 mm downstream.

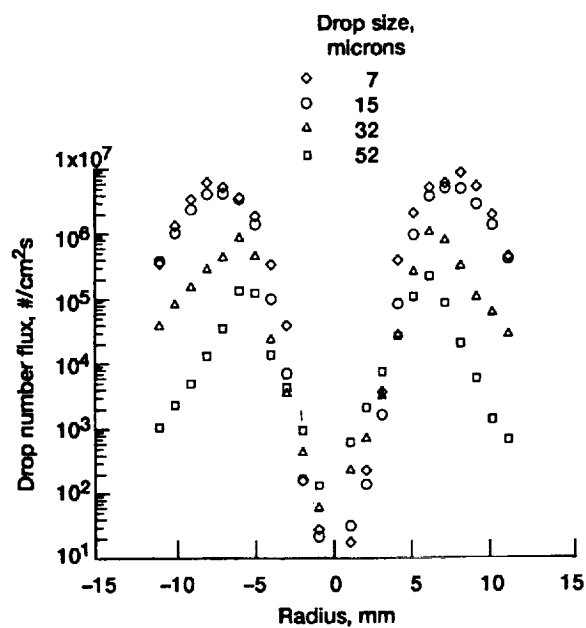


Figure 7.—Drop number flux at 5 mm downstream.



Figure 8.—Particle traces for turbulent backward-facing step flow.

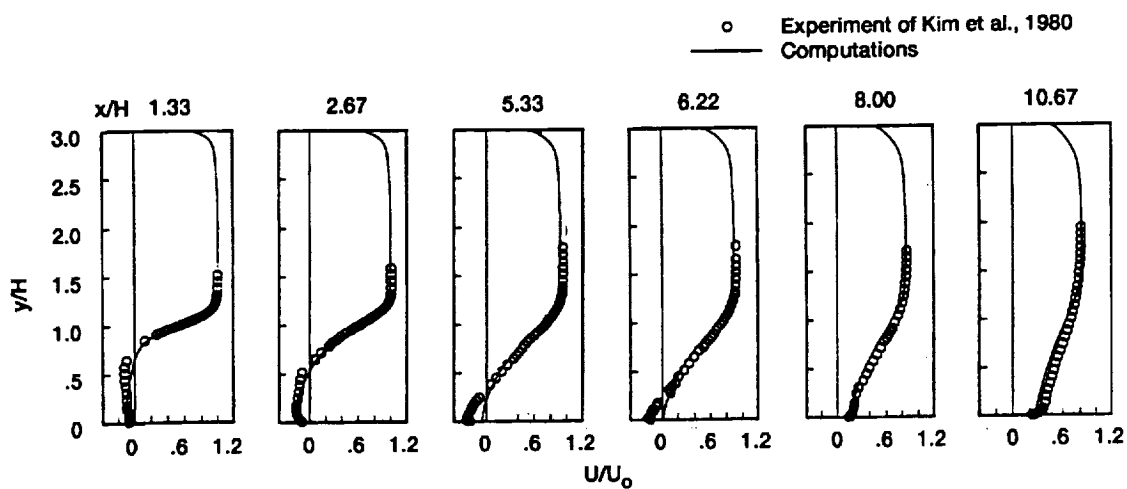


Figure 9.—Numerical predictions of the mean velocity profiles at selected axial locations for the turbulent backward-facing step flow.

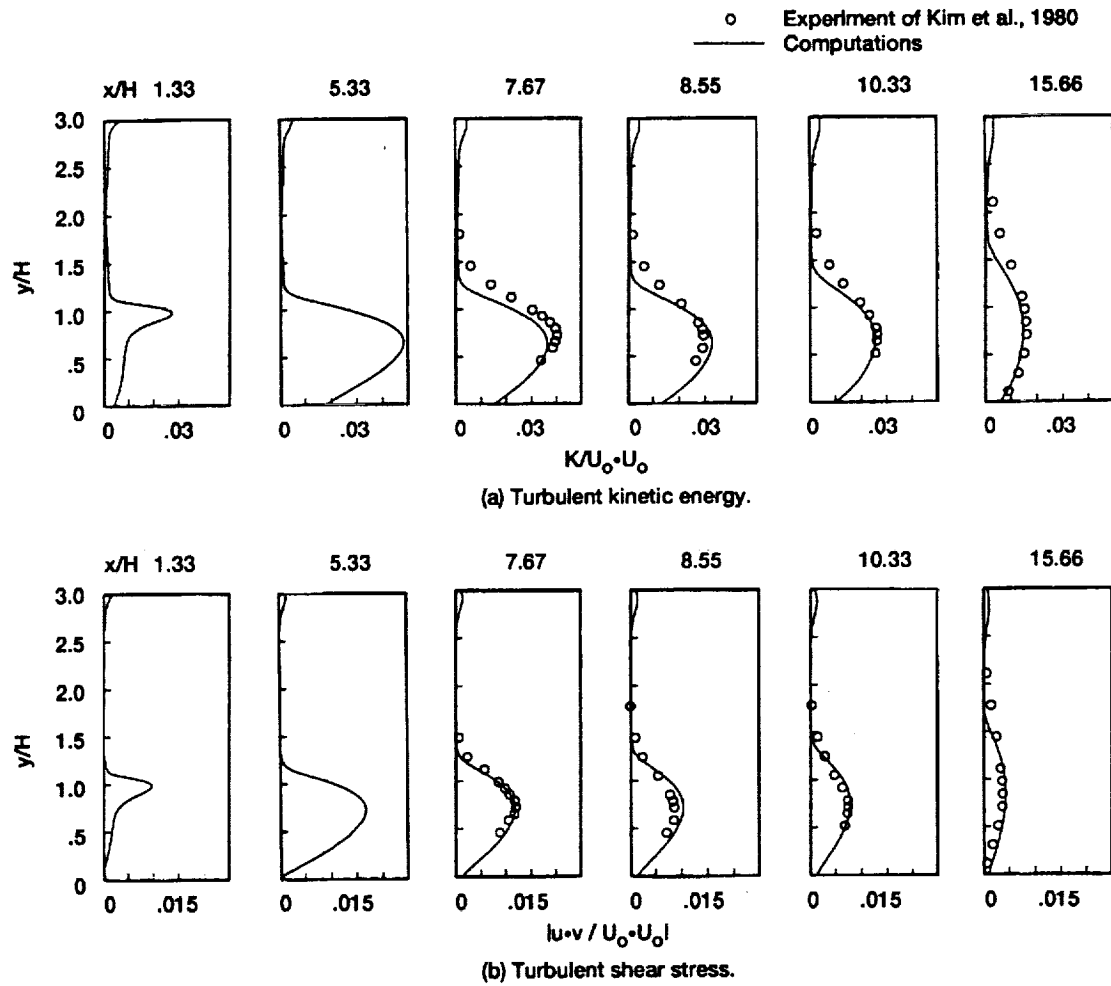


Figure 10.—Comparisons of (a) turbulent kinetic energy and (b) turbulent shear stress at some selected axial locations for the turbulent backward-facing step flow.

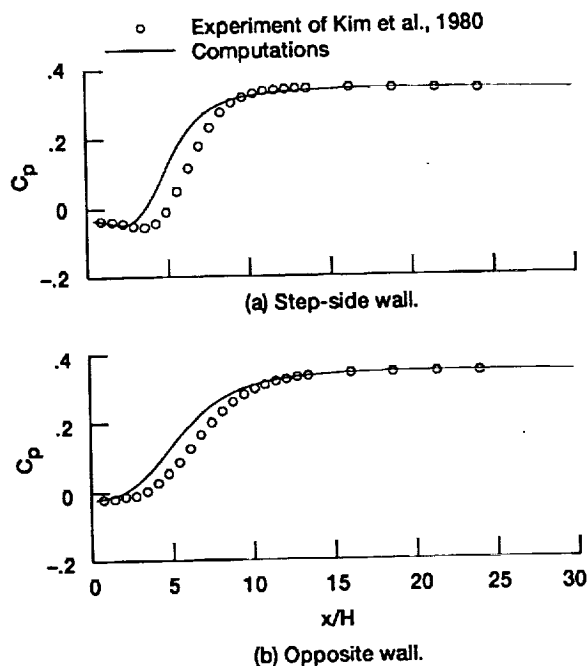


Figure 11.—Comparison of the wall pressure coefficients for the turbulent backward-facing step flow.

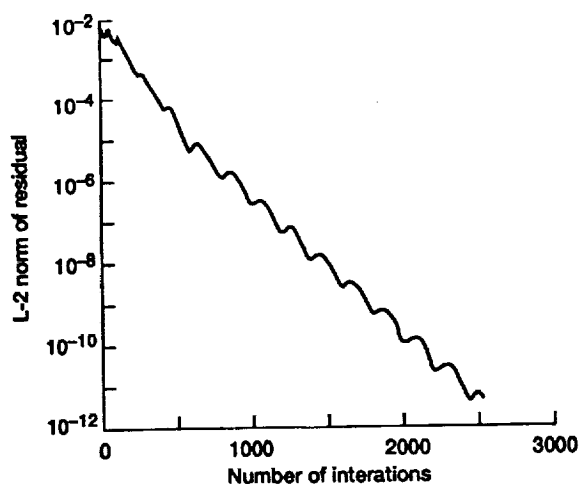


Figure 12.—Convergence history for the turbulent backward-facing step flow.

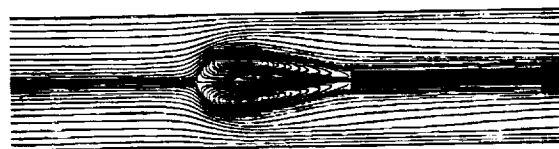


Figure 13.—Particle traces for the reverse jet combustion flow.

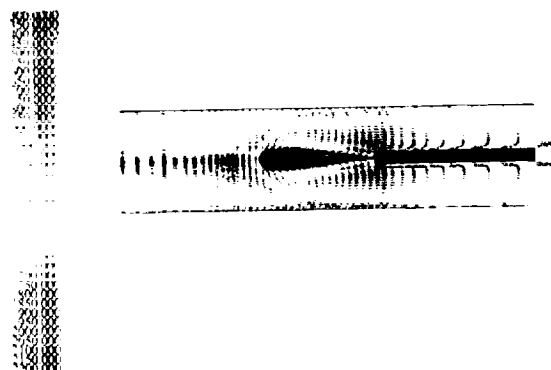


Figure 14.—Velocity vectors (colored by temperature) for the reverse jet combustion flow.

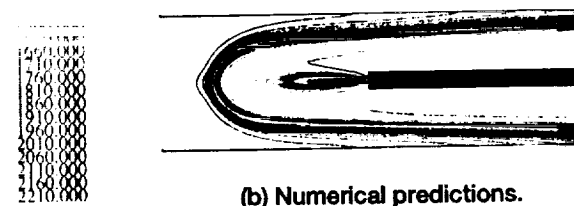
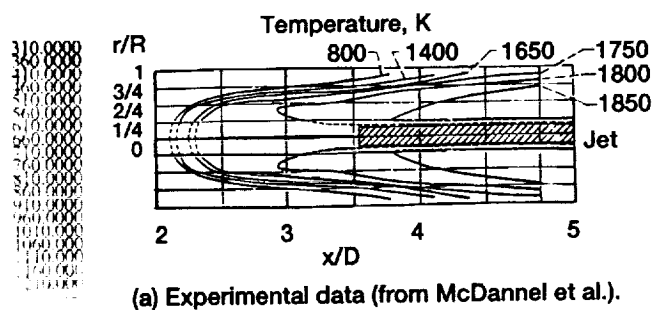


Figure 15.—Comparison of the temperature predictions with the experimental data for the reverse jet combustion flow.



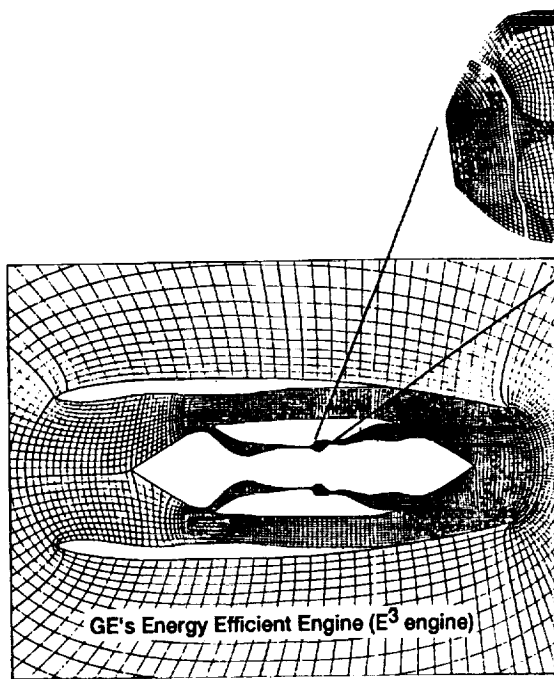


Figure 16.—Center-plane cut for GE's EEE gas turbine engine and the grid for the 2-D combustor.

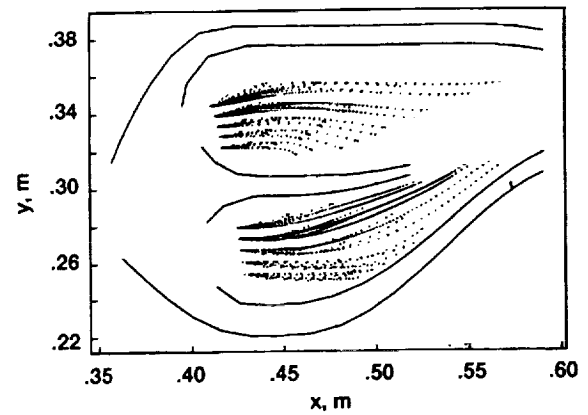
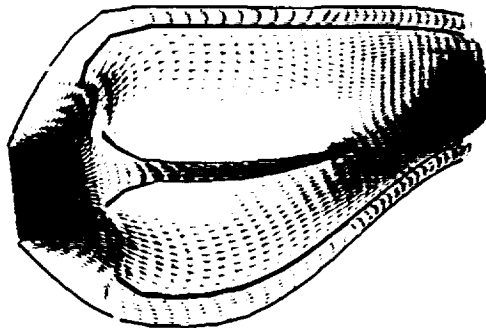
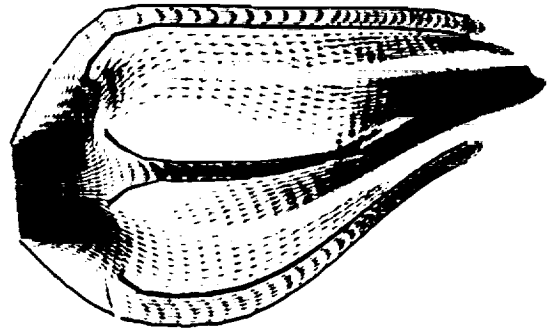


Figure 17.—Liquid fuel particle trajectories for the 2-D gas turbine spray combustion flow.

CONTOUR LEVELS  
 7450.0000  
 7500.0000  
 7550.0000  
 7600.0000  
 7650.0000  
 7700.0000  
 7750.0000  
 7800.0000



(a) Non-combustion flow (cold flow, no spray).



(b) Spray combustion flow.

Figure 18.—Velocity vectors (colored by temperature) for (a) non-combustion and (b) spray combustion cases for the 2-D gas turbine spray combustion flow.



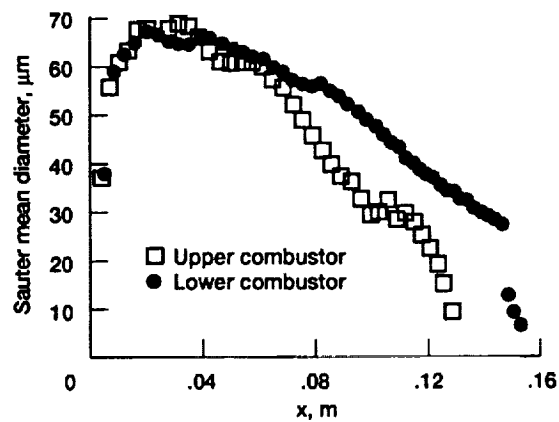


Figure 19.—Sauter mean diameter distribution for upper and lower combustor domes along the averaged trajectory for the 2-D gas turbine spray combustion flow.

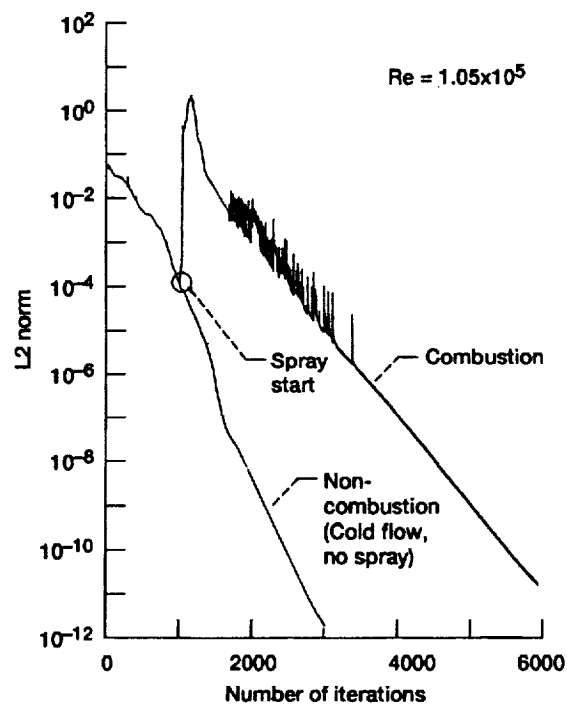


Figure 20.—Convergence history for both non-combustion and spray combustion cases for the 2-D gas turbine spray combustion flow.

REPORT DOCUMENTATION PAGE			Form Approved OMB No. 0704-0188	
Public reporting burden for this collection of information is estimated to average 1 hour per response, including the time for reviewing instructions, searching existing data sources, gathering and maintaining the data needed, and completing and reviewing the collection of information. Send comments regarding this burden estimate or any other aspect of this collection of information, including suggestions for reducing this burden, to Washington Headquarters Services, Directorate for Information Operations and Reports, 1215 Jefferson Davis Highway, Suite 1204, Arlington, VA 22202-4302, and to the Office of Management and Budget, Paperwork Reduction Project (0704-0188), Washington, DC 20503.				
1. AGENCY USE ONLY (Leave blank)	2. REPORT DATE Spring 1993	3. REPORT TYPE AND DATES COVERED Technical Memorandum		
4. TITLE AND SUBTITLE Spray Combustion Experiments and Numerical Predictions		5. FUNDING NUMBERS  WU-505-62-52 1L161102AH45		
6. AUTHOR(S) Edward J. Mularz, Daniel L. Bulzan, and Kuo-Huey Chen				
7. PERFORMING ORGANIZATION NAME(S) AND ADDRESS(ES) NASA Lewis Research Center Cleveland, Ohio 44135-3191 and Vehicle Propulsion Directorate U.S. Army Research Laboratory Cleveland, Ohio 44135-3191		8. PERFORMING ORGANIZATION REPORT NUMBER  E-7647		
9. SPONSORING/MONITORING AGENCY NAMES(S) AND ADDRESS(ES) National Aeronautics and Space Administration Washington, D.C. 20546-0001 and U.S. Army Research Laboratory Adelphi, Maryland 20783-1145		10. SPONSORING/MONITORING AGENCY REPORT NUMBER  NASA TM-106069 ARL-MR-69		
11. SUPPLEMENTARY NOTES Prepared for the AGARD Symposium on Fuels and Combustion Technology for Advanced Gas Turbine Engines sponsored by the Advisory Group for Aerospace Research and Development, Colleferro, Nr. Rome, Italy, Spring 1993. Edward J. Mularz, Vehicle Propulsion Directorate, U.S. Army Research Laboratory, Cleveland, Ohio; Daniel L. Bulzan, NASA Lewis Research Center; and Kuo-Huey Chen, University of Toledo, Toledo, Ohio 43606. Responsible person, Edward J. Mularz, (216) 433-5850.				
12a. DISTRIBUTION/AVAILABILITY STATEMENT  Unclassified - Unlimited Subject Categories 07 and 34		12b. DISTRIBUTION CODE		
13. ABSTRACT (Maximum 200 words)  The next generation of commercial aircraft will include turbofan engines with performance significantly better than those in the current fleet. Control of particulate and gaseous emissions will also be an integral part of the engine design criteria. These performance and emission requirements present a technical challenge for the combustor: control of the fuel and air mixing and control of the local stoichiometry will have to be maintained much more rigorously than with combustors in current production. A better understanding of the flow physics of liquid fuel spray combustion is necessary. This paper describes recent experiments on spray combustion where detailed measurements of the spray characteristics were made, including local drop-size distributions and velocities. Also, an advanced combustor CFD code has been under development and predictions from this code are compared with experimental results. Studies such as these will provide information to the advanced combustor designer on fuel spray quality and mixing effectiveness. Validation of new fast, robust, and efficient CFD codes will also enable the combustor designer to use them as additional design tools for optimization of combustor concepts for the next generation of aircraft engines.				
14. SUBJECT TERMS Combustion; Fuel sprays; CFD; Gas turbine combustors		15. NUMBER OF PAGES 25		
		16. PRICE CODE A03		
17. SECURITY CLASSIFICATION OF REPORT Unclassified	18. SECURITY CLASSIFICATION OF THIS PAGE Unclassified	19. SECURITY CLASSIFICATION OF ABSTRACT Unclassified	20. LIMITATION OF ABSTRACT	